Mechanistic insights into hydrogen evolution from methanol photoreforming on metal-loaded anatase: Development of a microkinetic model

Matthew J. Wigglesworth [a], Ruiman Ma [a], Natalia Martsinovich [b], Sergio Vernuccio [c,*]

[a] School of Chemical, Materials and Biological Engineering, University of Sheffield, United Kingdom
[b] Chemistry, School of Mathematical and Physical Sciences, University of Sheffield, United Kingdom
[c] School of Chemistry and Chemical Engineering, University of Southampton, United Kingdom

A B S T R A C T

A microkinetic model was developed to describe the kinetics of hydrogen production via methanol photoreforming under UV and visible light irradiations. The model integrates DFT calculations with experimental results to uncover mechanistic insights on the photoreforming process. The reaction mechanism and its governing rate coefficients were embedded into the design equation of a batch reactor to simulate the experimentally measured hydrogen evolution rates. Methanol exhibits a moderate reaction barrier to the methoxy anion (0.39 eV) and a low barrier to formaldehyde (0.16 eV), which serves as a key intermediate enabling multiple reaction pathways. In contrast, water shows moderately accessible formation of the hydroxyl radical (reaction barrier: 0.43 eV) while the formation of oxygen radicals is less accessible (reaction barrier: 0.66 eV). Radical coupling results in the exothermic formation of formic acid. Direct oxidation of formaldehyde yields carbon monoxide, whereas its hydroxylation leads to the formation of carbon dioxide. The microkinetic model incorporating DFT-derived energies showed good agreement with experimental methanol photoreforming data. The production of CH_2O closely follows that of H_2, emerging as the most kinetically accessible oxidation pathway. The production of O_2 is predicted to be negligible across all metals, and the production of CO and CO_2 is predicted to be minimal. These findings demonstrate the power of microkinetic modelling methodologies to accurately predict photocatalytic behaviour and guide the rational design of more efficient hydrogen evolution systems.

1. Introduction

Since the idea of photocatalytic water splitting powered by solar energy was theorised by Honda-Fujishima [1], it has remained of great interest as a desirable route to clean hydrogen production. However, its practical applications remain limited due to low solar-to-hydrogen efficiencies and hydrogen production rates [2]. Challenges in photocatalysis arise from the limitations of many semiconductor materials, including wide band gaps, poor electron-hole separation, and poor exciton migration to the surface. Several strategies including semiconductor surface loading with noble metals [3] [4] [5] [6] [7], Z- and S-schemes [8] [9] [10] [11] and various p-n heterojunction systems [12] [13] [14] have been explored in an attempt to mitigate these issues. However, none have yet resulted in an economically viable solution suitable for large-scale hydrogen production.

Despite these limitations, research efforts have increasingly focused on identifying and optimising semiconductor materials to overcome these issues. Among them, TiO_2 is a typical and widely researched material in the field of photocatalysis, which still receives considerable attention [15] [16] [17]. It primarily exists as two crystalline phases – rutile and anatase – with a third, less common phase known as brookite [18]. Among these, anatase is generally considered as the most photoactive phase with a band gap (E_g) of 3.2 eV [19] [20] [21] and therefore, it is frequently employed as a model system in photocatalytic research [22] [23] [24] [25] [26]. Photocatalytic water splitting is a key reaction studied using TiO_2 [27] [28] [29] [30] [31] [32] [33] where the production of H_2 from water-splitting is driven by the irradiation of a photocatalyst generating electron-hole (e^--h^+) pairs. The photogenerated holes facilitate the oxidation of adsorbed H_2O molecules, yielding protons (H^+) and oxygen (O_2), while the photogenerated electrons reduce H^+ to produce hydrogen (H_2) [34]. However, the overall efficiency of this reaction is often limited by the rapid recombination of charge carriers and the thermodynamically favourable backward reaction, which forms water from its dissociated state. The introduction of a sacrificial agent, such as methanol (CH_3OH), enables irreversible scavenging of holes, thereby enhancing the H_2 production rate [35] [36] [37] [38].

The incorporation of metal co-catalysts onto anatase has gained considerable attention over the years to improve its photocatalytic performance [39] [40] [41]. These co-catalysts serve as charge trapping

sites, significantly enhancing photocatalytic efficiency, although their effectiveness is highly dependent on factors such as metal selection [42] [43] and loading concentration [44] [45]. In a recent study, we integrated computational and experimental techniques to shed light on how different noble metals such as Pt, Pd, Au, and Ag affect the photocatalytic enhancement of TiO$_2$ activity for hydrogen production via methanol reforming [46]. Despite these insights, a comprehensive mechanistic understanding of the reaction pathway remains essential for accurately predicting hydrogen evolution and guiding the rational design of more effective photocatalysts.

Mechanistic studies using quantum mechanical methodologies are crucial for interpreting experimental phenomena at the atomic level, elucidating reaction barriers, electronic structure, and adsorption energies [47] [48] [49] [50] [51] [52]. When integrated with experimental studies, these theoretical approaches enable a comprehensive understanding of reaction mechanisms [53] [54] [55] and identification of catalyst descriptors for further catalyst development [56] [57]. Modelling approaches, building upon these quantum mechanical insights, offer a complementary framework to translate atomic-level information into a dynamic description of the catalytic process. Microkinetic modelling, in particular, is based on the construction of a reaction network composed by elementary steps that adhere to the principle of microscopic reversibility, without requiring any a priori identification of rate-determining steps. Estimating rate coefficients from density functional theory (DFT) calculations provides a rigorous basis for elucidating the reaction mechanism, enabling the quantification of transient intermediates and product distributions within the reaction network. These models have been broadly applied to catalytic transformation over transition metals [58] [59], zeolites [60] [61], and metal oxides [62] [63] [64]. However, the application of microkinetic modelling to photocatalytic transformations remains limited. Kovacic et al. [65] incorporated electronic excitation effects in their modelling of CO$_2$ photoreduction over Cu/TiO$_2$. Solé-Daura et al. [66] combined spectroscopic techniques with DFT and microkinetics in their modelling of CO$_2$ reduction using metal-organic frameworks. Other studies have addressed systems such as methane to methanol conversion [67] and C—H bond activation [68] [69]. To date, however, no studies have applied microkinetic modelling to investigate photocatalytic hydrogen production. This study introduces the first experimentally validated microkinetic model to describe the kinetics of methanol photoreforming for hydrogen production, offering insights at the mechanistic level. TiO$_2$ is used as a model photocatalyst, coupled with noble metal co-catalysts such as Pt, Pd, Au, and Ag, to form characteristic Schottky heterojunctions that enhance charge separation and photocatalytic performance.

The paper is structured as follows: Section 2 outlines the computational and experimental methodology, encompassing DFT calculations, microkinetic model development, and experimental hydrogen evolution. In Section 3.1 we elucidated the full photoreforming mechanism, including methanol oxidation to formaldehyde, carbon monoxide, and carbon dioxide, as well as water splitting. In Section 3.2 we provided a general description of the reaction kinetics by presenting the results of the microkinetic modelling with experimental validation and reaction pathway analysis.

2. Methods and materials

2.1. Computational methods

2.1.1. DFT calculations

DFT calculations were performed using the 5.4.4 version of the Vienna Ab initio Simulation Package (VASP) [70] [71]. The Generalised Gradient Approximation (GGA) with the Perdew-Burke-Ernzerhof functional (PBE) was employed to compute exchange-correlation energies in all calculations [72]. The Projector Augmented Wave (PAW) method was used to describe the inner electrons [73] [74], with a cutoff energy of the plane-wave basis set of 520 eV. Molecules in the gas phase were calculated in boxes with dimensions 8x8x8 Å. Van der Waals interactions were accurately captured by including Grimme's DFT-D3 dispersion correction method, combined with the Becke-Johnson (BJ) damping approach for interatomic distances [75] [76]. To address electron self-interaction within the semiconductor material, corrections were applied using the Coulomb interaction U and the electronic exchange J within Dudarev's GGA + U framework [77]. A U value of 3.9 eV was used as suggested by previous literature [50]. The lattice parameters for the anatase structure were optimized to be $a = 7.49$ Å and $b = 10.47$ Å. The (101) surface is widely recognised as the most thermodynamically stable facet of anatase [78] and is typically the predominant exposed surface under standard synthesis conditions [79] [80]. Accordingly, our catalyst was modelled as a Ti$_{24}$O$_{48}$ anatase (101) supercell to replicate the bulk lattice structure (Fig. S2), in line with numerous theoretical studies reported in the literature [81] [82] [83] [84] [85] [86]. The (101) surface was chosen as the preferential exposure of anatase nanocrystals according to X-ray diffraction analyses reported in our previous work [46]. A 5x5x1 Gamma point grid was used to sample the Brillouin zone. A vacuum height of 20 Å was used to prevent spurious interactions with neighbouring slabs. The convergence criteria for all optimisation calculations were set at 1×10^{-6} eV for the self-consistent field and 0.01 eV/Å for atomic forces. To achieve structural optimization, a conjugate-gradient optimisation method was employed.

For frequency calculations, the self-consistent field convergence criterion was set to 1×10^{-7} eV. Transition states were determined using the Nudged Elastic Band (NEB) method [87], implemented with the VTST toolkit [88]. Convergence criteria for all NEB images were set at 1×10^{-7} eV for the self-consistent field and 0.05 eV/Å for the atomic forces. The Vaspkit code was used to apply thermal corrections to the Gibbs free energy [89]. We assessed the sensitivity of our results to solvation by applying an implicit solvation model [90] using a polar medium with a water-like dielectric constant ($\varepsilon = 78.35$) as the solvent. The thermodynamic and kinetic properties of methanol oxidation in the presence of the solvent remained largely unaffected compared to vacuum calculations.

The Gibbs free energy change associated with a generic reaction step (ΔG_{rxn}) was calculated as:

$$\Delta G_{rxn} = \Delta E_{rxn} + \Delta E_{ZPE} - T \cdot \Delta S_{rxn} \tag{1}$$

Where ΔE_{ZPE} and ΔS_{rxn} are the difference in zero-point energy (ZPE) and difference in entropy between products and reactants, respectively. T is the temperature of 298 K. ΔE_{rxn} represents the total energy change between products and reactants for the generic reaction step. For instance, the adsorption energy of a molecular species (adsorbate) onto the surface of TiO$_2$ (ΔE_{ads}) was calculated as:

$$\Delta E_{ads} = E_{adsorbate@TiO_2} - (E_{adsorbate} + E_{TiO_2}) \tag{2}$$

where $E_{adsorbate@TiO_2}$ is the energy of the adsorbate on the TiO$_2$ surface, $E_{adsorbate}$ is the energy of the molecular species, and E_{TiO_2} is the energy of the pristine TiO$_2$ surface.

2.1.2. Microkinetic model development

A microkinetic model was developed to integrate insights from experimental findings and computationally derived rate coefficients, providing a detailed kinetic characterization of the photoreforming

mechanism. Each elementary reaction step was assumed to be reversible, with no a priori assumption on the rate determining step. Thus, the rate constants for forward reaction steps $k_\rightarrow$ were expressed according to the transition state theory [91]:

$$k_\rightarrow = \frac{k_B T}{h} e^{\frac{-\Delta G_\rightarrow^\ddagger}{RT}} \qquad (3)$$

Where k_B is the Boltzmann constant, T is the temperature, h is the Planck constant, $\Delta G_\rightarrow^\ddagger$ is the activation free energy obtained as the Gibbs free energy difference between the transition state and the reactants, and R is the universal gas constant.

To ensure thermodynamic consistency of the microkinetic model, the rate coefficients of the reverse reactions $k_\leftarrow$ were calculated as:

$$k_\leftarrow = \frac{k_\rightarrow}{K_{eq}} \qquad (4)$$

Where K_{eq} was expressed as:

$$K_{eq} = e^{\frac{-\Delta G_{rxn}}{RT}} \qquad (5)$$

Adsorption steps were assumed to be enthalpically unactivated. Therefore, the rate coefficients for the adsorption steps k_{ads} were expressed as:

$$k_{ads} = \frac{k_B T}{h} e^{\frac{\Delta S_{ads}^\ddagger}{R}} \qquad (6)$$

The rate coefficients for the desorption steps were calculated from DFT-derived adsorption energies. The entropy change $\Delta S_{ads}^\ddagger$ was estimated using the approach proposed by Campbell and Sellers [92], assuming that the transition state for adsorption experiences an entropy loss equivalent to one-third of the translational entropy of the molecule in the gas phase (S_{trans}^o), calculated as [93]:

$$S_{trans}^o = R \left[ln \left(\left(\left(\frac{2\pi M k_B T}{h^2} \right)^{3/2} \right) \frac{k_B T}{p^o} \right) + \frac{5}{2} \right] \qquad (7)$$

Where p^o is the standard pressure and M is the molecular mass of the species. The vibrational and rotational entropies were assumed to remain unchanged between the free molecule and the adsorbed phase, implying that the entropy change is solely attributed to the loss of translational entropy.

2.2. Experimental methods

2.2.1. Materials

Titanium (IV) oxide (anatase nanopowder, particle size <25 nm, density 3.9 g•mL^{-1}, specific surface area 45–55 m^2•g^{-1}, 99.7 %), palladium (II) chloride (PdCl$_2$, $\geq$ 99.9 %), silver nitrate (AgNO$_3$, ACS reagent, $\geq$ 99.0 %), gold (III) chloride trihydrate (AuCl$_3$•3H$_2$O, $\geq$99.9 % trace metals basis), chloroplatinic acid hexahydrate (H$_2$PtCl$_6$•6H$_2$O, ACS reagent, $\geq$ 37.50 % Pt basis) and methanol (99 %) were obtained from Sigma Aldrich. All reagents were used as received. All experiments employed doubly distilled water.

2.2.2. Photocatalytic experiments

Photocatalytic experiments were conducted at room temperature using a 300 mL annular glass batch reactor with a height of 40 cm and a diameter of 75 mm, following a previously reported procedure [94]. The reactor was equipped with a magnetic stirrer operating at 1200 rpm and

a light source enclosed in a quartz jacket. The stirring speed was selected to ensure homogeneous mixing of the reaction solution and to eliminate any external mass transfer limitations (see Section S1 of the Supporting Information).

A 400 W medium-pressure mercury (Hg) lamp (Photochemical Reactors Ltd) served as the light source. The lamp primarily emits UV light irradiations at 302, 313, 334, and 366 nm, and visible light irradiations at 406 and 436 nm (manufacturer's data). The lamp's effective irradiances were determined using a Delta OHM HD2102.1 photo-radiometer fitted with two probes, covering the 0–400 nm and 400–1000 nm wavelength ranges. The measured irradiances at 302, 313, 334, 366, 406, and 436 nm were 1.17×10^{-6}, 3.19×10^{-6}, 3.41×10^{-7}, 6.97×10^{-6}, 3.04×10^{-5}, and 6.62×10^{-5} Ein•s^{-1}, respectively. Radiations below 300 nm were filtered out using a cut-off filter.

In a typical run, 150 mg of TiO$_2$ and selected concentrations of noble metal precursors were dispersed in 0.3 L of unbuffered doubly distilled water solution containing methanol in the concentration range 0.0–3.0 M. The Schottky metal/TiO$_2$ heterojunctions (metal concentration of 0.5 mol%) were prepared through in-situ photodeposition. Resulting materials were extensively characterized in our previous work using a comprehensive suite of techniques to investigate their structural, morphological, and optical properties [46].

To maintain an oxygen-free environment in the reactor, nitrogen gas was purged through the solution for 40 min prior to initiating the photocatalytic reaction, effectively eliminating the possibility of interactions between dissolved oxygen and photogenerated electrons. During the entire reaction process, nitrogen gas was continuously supplied at a flow rate of 1 L•min^{-1} and cooling water was continuously circulated through the lamp jacket to prevent overheating of the lamp. Gas samples were collected at various time intervals using 1 L Tedlar sampling bags and analysed using a Thermo Scientific Trace 1310 gas chromatograph. The instrument was fitted with a HS-Q column (2 m, 60/80 mesh) and a thermal conductivity detector (TCD), with argon employed as the carrier gas for all analyses.

The Weisz-Prater criterion was applied to confirm that the experimental results reflect the intrinsic kinetics of the process without interference from internal (intraparticle) diffusion (see Section S2 of the Supporting Information).

3. Results and discussion

3.1. Reaction mechanism

Due to the vast range of possible products arising from radical coupling, simulations of elementary steps were restricted to a selection of representative reactions. In this study, a reaction network was constrained to C$_1$ products, reflecting the fast conversion of radical species, as well as the low concentration of hydroxyl radicals on the anatase surface, which suggests that any heavier products are likely to have negligible concentration. Key elementary reaction steps describing the oxidation of methanol and water are displayed in Fig. 1 and analysed in detail in Sections 3.1–3.4. Methanol, water, and the reaction intermediates interact with the surface as adsorbed species on five-coordinated Ti atoms (Ti$_{5c}^{4+}$) [22] [95]. The recombination of the hydrogen radicals occurs on the transition metal sites (TM) [96] [97] [98].

The oxidation of methanol to formaldehyde has been extensively studied [50] [99] [100] [101] [102] and is deemed to proceed through two initial pathways: thermal dissociation followed by hole assisted cleavage, or radical assisted cleavage. Water can form a hydroxyl radical
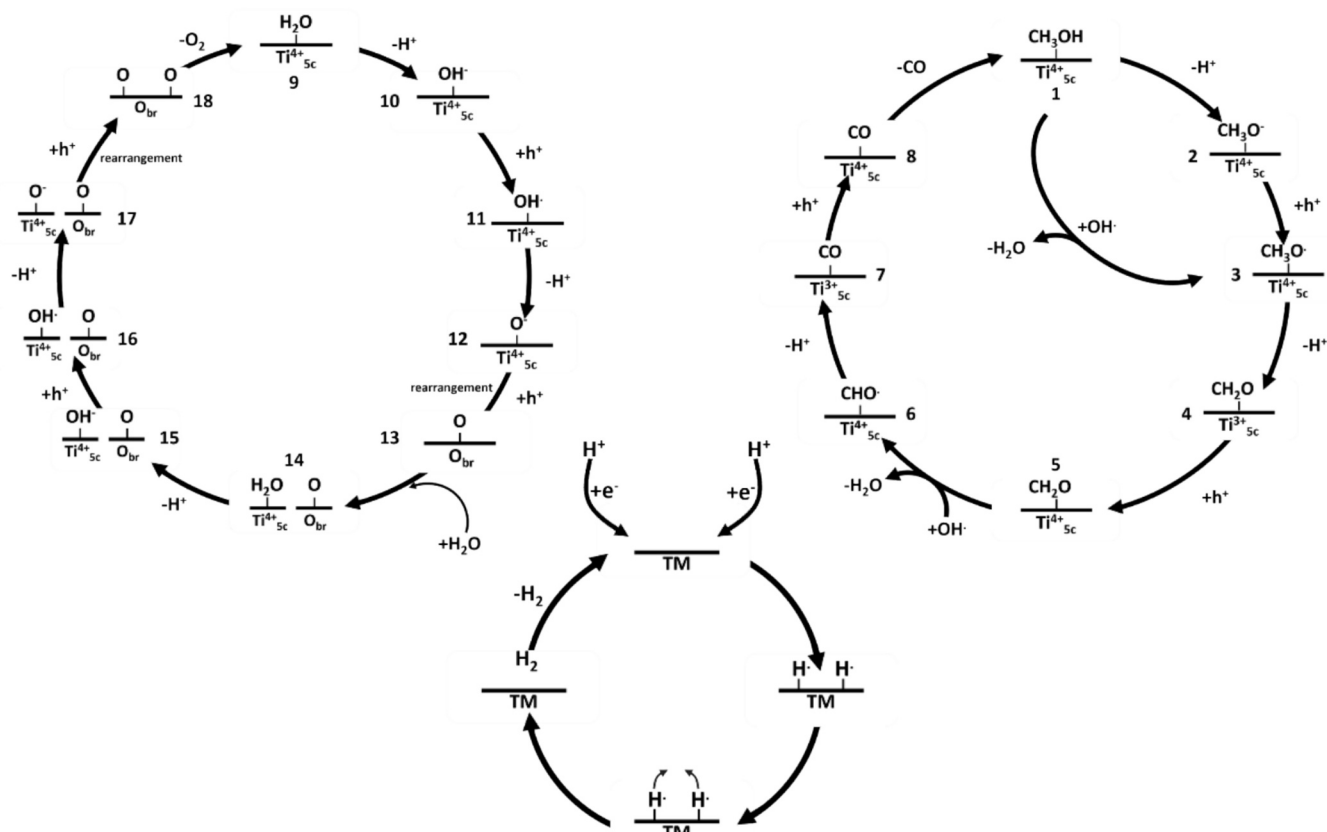
Fig. 1. Schematic illustration of the key elementary steps in the hydrogen production process through simultaneous oxidation of methanol and water on the (101) anatase surface.

which can further oxidise to oxygen radicals or undergo radical coupling to form hydrogen peroxide, which can then decompose to molecular oxygen. The oxidation of formaldehyde can yield methanediol ($CH_2(OH)_2$) or a formyl radical (CHO) as reaction intermediates. Methanediol undergoes oxidation to form formic acid (CHOOH), which subsequently converts to carbon dioxide (CO_2). Alternatively, the formyl radical can be oxidised to carbon monoxide (CO) or undergo radical coupling with a hydroxyl radical to form formic acid.

3.1.1. Methanol oxidation to formaldehyde

Fig. 2 shows dissociation of adsorbed CH_3OH via hydrogen bonding of the methanol hydrogen to the O_{br} site (*I-III*, Fig. 2b), resulting in the formation of a CH_3O^- anion on Ti_{5c}^{4+} (step 1–2, Fig. 1). The first deprotonation step of an adsorbed CH_3OH is an endergonic heterolytic cleavage with an energy barrier of 0.39 eV (Fig. 2a). The corresponding backward reaction step has a barrier of 0.18 eV. The low reverse barrier arises from the comparatively weaker stabilisation of the charged fragments on the anatase surface relative to that of the methanol molecule. The resulting CH_3O^- anion binds strongly to the Ti_{5c}^{4+} atom, with a Ti_{5c}^{4+}–O bond length of 1.86 Å (*III*, Fig. 2b). A theoretical study of methanol dissociation on rutile by Zhang et al. [103] found that the initial dissociation step is primarily driven by thermal activation rather than photoactivated. This is because the photogenerated hole from

photon excitation becomes trapped at an O_{br} site next to the adsorbed methanol; the presence of a hole on the O_{br} site reduces the Coulombic attraction between this oxygen and methanol hydrogen, leading to an increased energy barrier for methanol O—H dissociation. They concluded that the hole did not facilitate the O—H dissociation process but was involved in the next step of C—H bond cleavage. Therefore, after the initial O—H bond cleavage step, a photogenerated hole was added to our simulation system. The photogenerated hole oxidises the CH_3O^- anion (step 2–3, Fig. 1), generating a $CH_3O^\bullet$ radical (*IV*, Fig. 2b) and extending the Ti_{5c}^{4+}–O bond to 2.07 Å (Fig. 2(b)). Once the hole is successfully trapped on the adsorbate, the dissociation of the C—H bond becomes favourable, with a low energy barrier of 0.16 eV. This is due to a change in the surface orientation of the $CH_3O^\bullet$ structure, which allows for a more kinetically feasible transition state (*VI*, Fig. 2b) via the elongation and subsequent cleavage of the C—H bond, while maintaining sufficient stability through a temporary hydrogen bond to the O_{br} site. During the dissociation process, the Ti_{5c}^{4+} site accepts an electron from the $CH_3O^\bullet$ radical and is reduced to Ti_{5c}^{3+} (structure 4, Fig. 1). As the C—H bond breaks, the newly formed CH_2O binds weakly to the Ti_{5c}^{3+} site (*VII*, Fig. 2b). Following C—H bond cleavage, the Ti_{5c}^{3+} can accept a hole, and is regenerated as an active site (structure 5, Fig. 1, Fig. 2a).

An alternative pathway involves the interaction of the adsorbed methanol with pre-existing surface hydroxyl species on the surface of
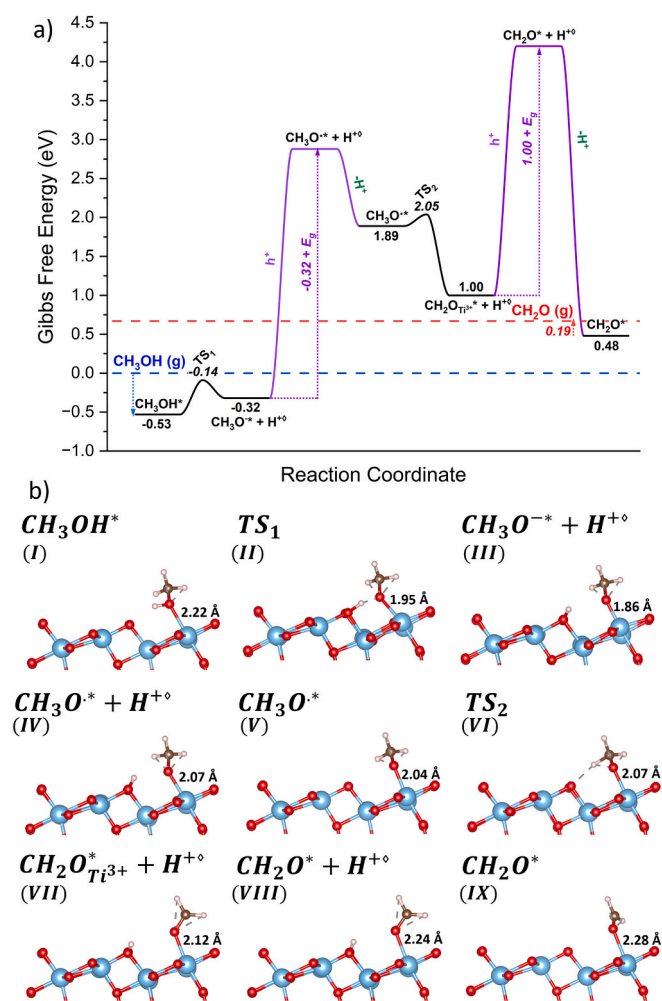
Fig. 2. (a) Reaction coordinate diagram describing the oxidation of methanol to formaldehyde over the (101) anatase surface. Surface species are adsorbed on Ti_{5c}^{4+}, unless specified. Protons are adsorbed on O_{br} sites. Black lines correspond to calculated Gibbs free energies. Purple lines correspond to gain/loss of charged species: photoexcitation processes (uphill step) which create a hole in TiO_2, followed by the loss of a proton (downhill step). The energy of the positively charged system after the addition of a hole and before the loss of a proton is represented by increasing the energy of the reactant system by the value of E_g (the band gap of the material, 3.2 eV [19] [20] [21]). In this and the following figures, species in the gas phase are denoted by (g). The horizontal blue and red dashed lines correspond to the energies of gas-phase methanol and formaldehyde, respectively. The symbols * and ◇ indicate the Ti and oxygen bridge active sites. (b) Optimized geometries of surface species and transition states with characteristic bond lengths. Atoms are coloured as follows: O (red), Ti (blue), C (brown), H (light pink).

TiO_2, as depicted in Fig. 3. The presence of the hydroxyl group on the surface facilitates methanol adsorption by lowering its binding energy to -0.68 eV. The adsorbed hydroxyl group interacts with a hydrogen atom of the alcohol group, forming a hydrogen bond with a length of 1.62 Å. This interaction facilitates the dissociation of hydrogen from methanol, occurring with a minimal activation barrier of 0.05 eV, and leading to the formation of a methoxy anion and water. The reverse reaction occurs with a slightly higher barrier of 0.16 eV. The formed $CH_3O^{\bullet}$ radical
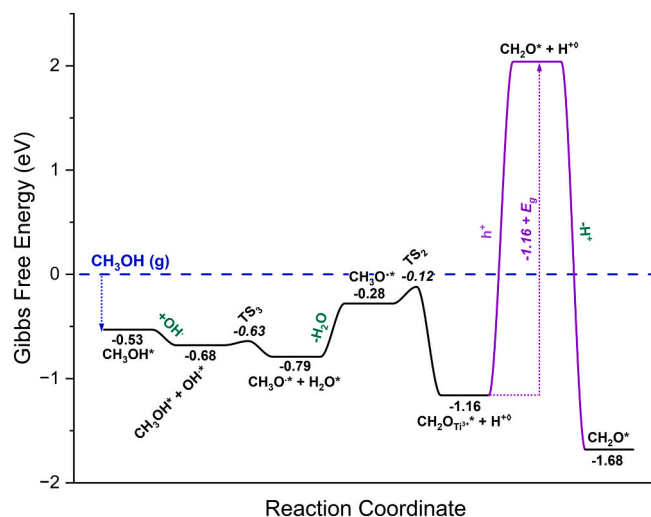

Fig. 3. Reaction coordinate diagram describing the oxidation of methanol to formaldehyde on the (101) anatase surface via a hydroxyl-assisted reaction pathway. Surface species are adsorbed on Ti_{5c}^{4+}, unless specified. Protons are adsorbed on O_{br} sites. Notation is the same as Fig. 2.

intermediate follows the same oxidation pathway to formaldehyde as described in Fig. 2. However, the methoxy radical formation pathway depicted in Fig. 3 is likely to be favoured compared to the one in Fig. 2, due to its lower barrier of the initial dissociation step facilitated by hydrogen bonding with surface hydroxyl and due to its overall exergonic nature. The availability of surface hydroxyls has a key role in promoting this facile pathway, highlighting the synergy between methanol and water.

3.1.2. Formaldehyde oxidation to carbon monoxide

The conversion of formaldehyde to carbon monoxide was considered to proceed via OH• assisted C—H cleavage (step 5–6, Fig. 1). This is based on a theoretical study by Tao et al. [104] which elucidated that OH• assisted C—H bond cleavage is energetically more favourable than cleavage mediated by photogenerated holes. During this process, the C—H bond undergoes spontaneous cleavage (*I-III*, Fig. 4b), making the reaction barrierless and exergonic by 0.13 eV (Fig. 4a), and yielding a formyl radical (CHO•) and water (structure 6, Fig. 1). The formyl radical binds weakly to the Ti site, with a bond length of 2.55 Å in the presence of water (*III*, Fig. 4b). The reaction proceeds towards CO formation through a second C—H dissociation (step 6–7, Fig. 1). In this step, the weakening of the Ti—O bond (*IV*, Fig. 4b) facilitates the transfer of the hydrogen atom to the O_{br} site, proceeding with an energy barrier of 0.03 eV. As CHO• dissociates, the Ti_{5c}^{4+} site accepts an electron, and is reduced to Ti_{5c}^{3+} (structure 7, Fig. 1). The resulting CO intermediate binds weakly to the Ti site with a Ti—O distance of 4.11 Å (*VI*, Fig. 4b). After accepting a photogenerated hole, Ti_{5c}^{3+} is reoxidised to Ti_{5c}^{4+}, further increasing the Ti—O distance to 4.34 Å (*VII*, Fig. 4b), and enabling CO desorption from the surface (structure 8, Fig. 1). The CO intermediate appears to be surface bound through a C—H interaction (2.03 Å), while the Ti—O distance is too long to be considered a bond. The inclusion of a photogenerated hole reduces the C—H interaction distance to 1.93 Å. In this reaction mechanism, all steps involved are either thermodynamically downhill, characterized by low activation barriers, or are photoactivated, suggesting that the pathway is mechanistically feasible.
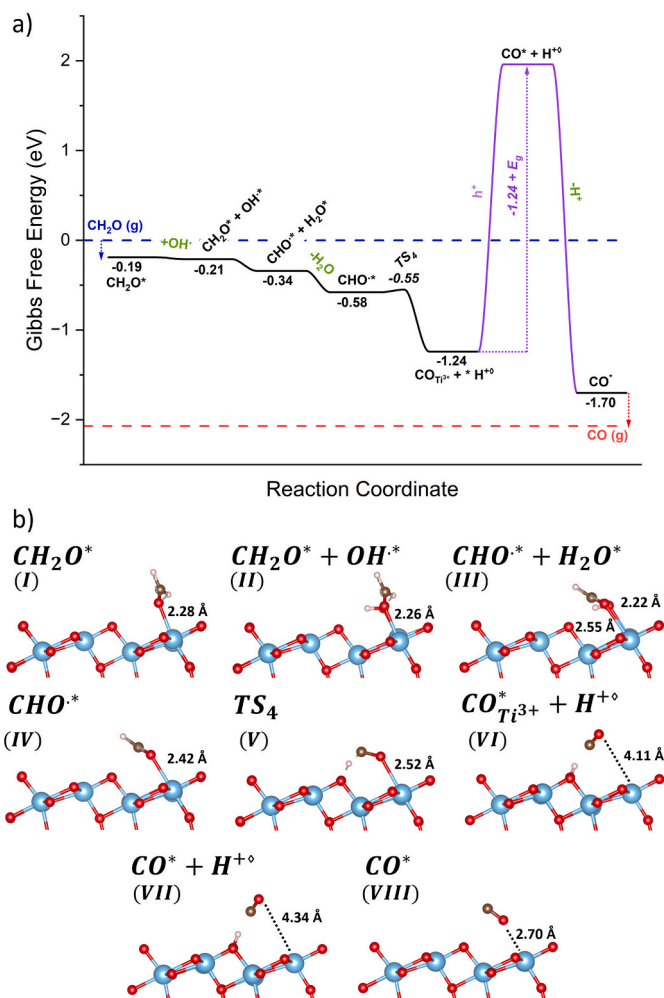
Fig. 5. Reaction coordinate diagram describing the overall water splitting reaction over the (101) anatase surface. Protons are adsorbed on O_{br} sites while the other surface species are adsorbed on Ti_{5c}^{4+}. Species in the gas phase are denoted by (g). * and ◇ indicate the Ti and oxygen bridge active sites. Notation is the same as Fig. 2, with the exception of the horizontal dashed lines representing water (blue) and oxygen (red) respectively.

Fig. 4. (a) Reaction coordinate diagram describing the oxidation of formaldehyde to carbon monoxide on the (101) anatase surface. Surface species are adsorbed on Ti_{5c}^{4+}, unless specified. Protons are adsorbed on O_{br} sites. (b) Optimized geometries of surface species and transition states with characteristic bond lengths. Notation is the same as Fig. 2, with the exception of the horizontal dashed lines representing formaldehyde (blue) and carbon monoxide (red) respectively.

3.1.3. Water oxidation

The competitive adsorption between water and methanol, coupled with the large excess of water in the reaction system, suggests that surface active sites are likely to be predominantly occupied by water. The first step in water oxidation is the dissociation of adsorbed H_2O (*I–III*, Fig. S4), which occurs via O—H heterolytic bond cleavage to yield OH^- and H^+ through an endergonic thermal process (step 9–10, Fig. 1, Fig. 5). The forward reaction exhibits a barrier of 0.43 eV, while the backward reaction has a lower barrier of 0.08 eV. The reduction in barrier for the reverse reaction compared to the dehydrogenation of CH_3OH presented in Section 3.1.1 can be attributed to the lack of a stabilising effect in the adsorbed hydroxyl. The methyl group on $CH_3O^•$ facilitates a redistribution of charge within the methoxy group, stabilising the adsorbed methoxy structure. Similar to CH_3OH oxidation, the transfer of a photogenerated hole to molecular H_2O is thermodynamically unfavourable due to the significantly higher valence band maximum of TiO_2 compared to the O_{2p} level of the adsorbed H_2O. Zhao et al. [105] reported that the activation barrier for O—H dissociation of water adsorbed on titania remains unchanged between a neutral and a positively charged system, indicating that the presence of a hole has a minimal impact on the O—H dissociation energy; this was attributed to the hole being localised on a nearby O_{br} site rather than on the reacting
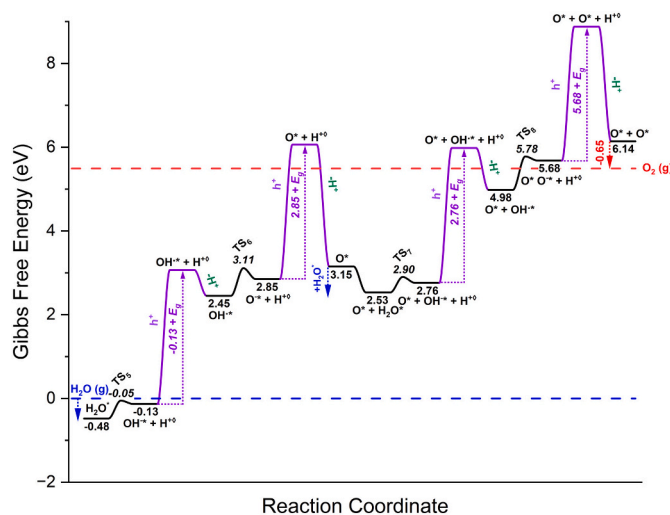
oxygen. The resulting hydroxyl anion (*III*, Fig. S4) captures the photogenerated hole (*IV*, Fig. S4), forming a hydroxyl radical (step 10–11, Fig. 1). Our results show that the second O—H dissociation step (*VI*, Fig. S4) occurs with a barrier of 0.66 eV, resulting in a proton loss and the formation of an oxygen adatom, which is 0.40 eV less stable than the adsorbed hydroxyl (11–12, Fig. 1). The high barrier and the more strongly endergonic nature of this reaction compared with methanol dehydrogenation or the first dehydrogenation of water, can be attributed to the small size of the oxygen anion and its limited ability to delocalise the negative charge. In addition, this reaction competes with the more rapid consumption of hydroxyl radicals by methanol and formaldehyde, making this pathway kinetically disfavoured. Once the oxygen adatom has formed, it can subsequently react with an O_{br} site (*IX*, Fig. S4), leading to the formation of a surface-bound peroxo intermediate (13, Fig. 1). At this stage, the release of O_2 is highly unfavourable due to the instability of the anatase surface with an oxygen vacancy. Instead, a second H_2O molecule can adsorb onto the surface (*X*, Fig. S4) near the peroxo species (structure 14, Fig. 1) and dissociate similarly to the first water molecule, releasing a proton, and forming an adsorbed OH^- anion (structure 15, Fig. 1, *XII*, Fig. S4). The peroxo group proceeds to cleave one of its Ti—O bonds by accepting a hole, resulting in the formation of a superoxo intermediate (Fig. S3). The second OH• group dissociates with a barrier of 0.80 eV, releasing its last proton (step 16–17, Fig. 1). This results in the remaining oxygen atom leaning towards the superoxo species and forming a bond with the first oxygen (step 17–18, Fig. 1). The two adsorbed O atoms can finally recombine to form an O_2 molecule (*XVII*, Fig. S4) and desorb from the TiO_2 surface, restoring the O_{br} site.

The formation of hydrogen peroxide on the surface of TiO_2 was additionally evaluated, as an alternative fate of adsorbed hydroxyl groups. Our results showed that the hydroxyl radicals are more stable when separated on the surface (Fig. S5) and that OH• is preferentially consumed by other reactions, suggesting the formation of hydrogen peroxide is minimal or negligible under the operating conditions investigated in this work.

3.1.4. Synergistic interactions between methanol and water in methanol oxidation to CO_2

As previously discussed, hydroxyl radicals generated from water dissociation, can promote both methanol and formaldehyde oxidation.
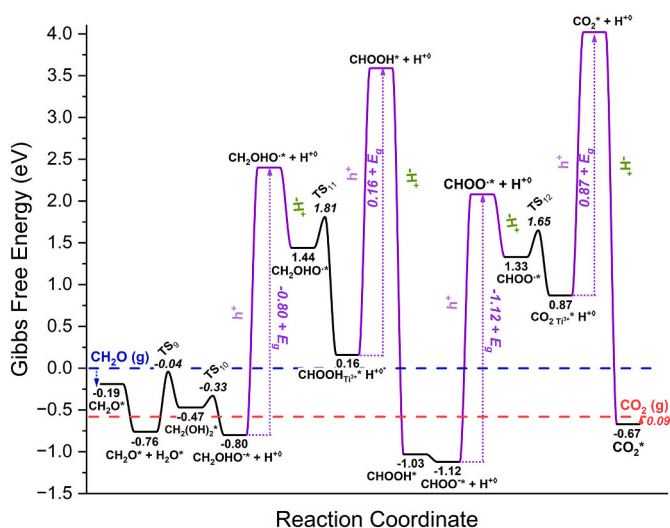
Fig. 6. Hydration of formaldehyde and its subsequent oxidation to CO_2 over the anatase (101) surface. Surface species are adsorbed on Ti_{5c}^{4+}, unless specified. Protons are adsorbed on O_{br} sites. Species in the gas phase are denoted by (g). The symbols * and ◇ indicate the Ti and oxygen bridge active sites. Notation is the same as Fig. 2, with the exception of the horizontal dashed lines representing formaldehyde (blue) and carbon dioxide (red) respectively.

Therefore, synergistic interactions of adsorbed methanol and water molecules both without and in the presence of hydroxyl radicals were included in the reaction network. CH_2O formed from methanol oxidation may either desorb as an intermediate product or undergo additional surface reactions. For instance, formaldehyde can capture a water molecule, forming a hydrated formaldehyde species (methanediol, Fig. S6). This reaction on TiO_2 proceeds with an activation barrier of 0.72 eV (Fig. 6), while the reverse reaction has a barrier of 0.43 eV, indicating that the hydration is endergonic. This may be attributed to the distances between the Ti_{5c}^{4+} active sites, which necessitates the dissociation of the Ti–H_2O bond before the water molecule can react with CH_2O. When both CH_2O and H_2O are co-adsorbed on the surface of TiO_2, their respective Ti—O bond lengths are 2.29 Å and 2.33 Å. This differs from the bond lengths observed during isolated adsorption interactions with the TiO_2 surface. The H_2O–Ti bond becomes weaker, with its length increasing from 2.26 Å. This suggests that the presence of CH_2O slightly influences the binding of H_2O to the TiO_2 surface. This effect is unlikely to arise from hydrogen bonding between the two molecular species; rather, it may be attributed to a stronger interaction between one of the H atoms in water and an O_{br} site. As a result, the H–O_{br} bond length decreases from 2.15 Å as an isolated adsorbed species, to 1.91 Å in the presence of CH_2O.

Methanediol may subsequently undergo thermal dissociation via heterolytic cleavage (Fig. S7) of an O—H bond with an activation barrier of 0.14 eV (Fig. 6). The reverse reaction has a barrier of 0.47 eV, indicating that the forward dissociation is exergonic, and that the CH_2OHO^- intermediate is thermodynamically more stable than the reactants. This can be attributed to the stronger hydrogen bonding between the adsorbate intermediate and the catalyst surface. A photogenerated hole can then be scavenged by the CH_2OHO^- intermediate, resulting in the formation of a $CH_2OHO^•$ radical (Fig. 6). This radical exhibits a significantly weaker interaction with the Ti site compared to the anion, with an O—Ti bond length of 1.85 Å for the anion and 2.07 Å for the radical. The weakening of the O—Ti bond is crucial for facilitating the kinetics of C—H bond dissociation. One of the C—H bonds is heterolytically cleaved with an activation barrier of 0.37 eV, and an electron is transferred from the dissociated CHOOH intermediate to the titania surface, reducing the Ti_{5c}^{4+} site to Ti_{5c}^{3+} and producing a neutral formic acid adsorbate. The subsequent interaction between the newly formed formic acid and the

reduced Ti site is weak, with a bond length of 2.27 Å. Following the dissociation, a photogenerated hole can regenerate the Ti_{5c}^{4+} site, while the cleaved proton readily leaves the TiO_2 surface. The resulting O—Ti bond length between the formic acid and the Ti_{5c}^{4+} site is 2.12 Å. Additionally, formic acid generation may also proceed via radical coupling between the formyl radical generated from step 6 in Fig. 1 and a hydroxyl radical, as illustrated in Fig. S8.

The formation of methanediol relies on the concentration of surface formaldehyde and a large excess of water but is hindered by a high reaction barrier. In contrast, the formation of formic acid via radical coupling is driven by the availability of surface hydroxyl radicals. The two mechanisms can coexist, with formic acid production likely to be the more favourable pathway. This reaction also competes with the formation of the CO intermediate as discussed in Section 3.1.2.

The oxidation of formic acid species to CO_2 follows a mechanism similar to the oxidation of methanol to formaldehyde and methanediol to formic acid. The process begins with the dissociation of the O—H bond, which occurs readily due to the strong hydrogen bonding between the hydrogen of the OH group of formic acid and the O_{br} site with a bond length of 1.42 Å. This interaction is substantially stronger than the corresponding O_{br}–H hydrogen bond observed with methanol (2.28 Å) and methanediol (2.27 Å), indicating that the O—H dissociation in formic acid is significantly more favourable than in these related species. The ease of O—H bond dissociation in formic acid is consistent with the higher acidity of the acid compared to the alcohol. As seen in Fig. 6, this reaction is effectively barrierless and slightly exothermic, with an energy release of 0.11 eV. Following O—H bond cleavage, the resulting $CHOO^-$ (formate) intermediate rotates (I to II, Fig. 7) to form a stable configuration that bridges two Ti_{5c}^{4+} sites, with Ti—O bond lengths of 2.09 Å. The introduction of a photogenerated hole to facilitate proton charge transfer slightly weakens the binding of the formate intermediate to the two Ti_{5c}^{4+} sites, increasing the Ti—O bond length to 2.12 Å (III, Fig. 7). The final oxidation step to CO_2 proceeds via an exergonic C—H bond dissociation step (V, Fig. 7), with an activation barrier of 0.23 eV. Upon CO_2 formation, the Ti—O bond length further weakens to 2.21 Å (VI, Fig. 7). The structure has a bent configuration, with an O=C=O bond of 139°, likely due to the reduced positive charge on the Ti_{5c} site. The introduction of a photogenerated hole in the system causes the release of CO_2 from the surface (VII, Fig. 7) and its transition to a linear structure, which maintains a single weak interaction with a Ti site (Ti—O bond length of 2.45 Å). Following the removal of the final proton, the CO_2 molecule rotates 90° horizontally (VIII, Fig. 7), resulting in a further increase of the bond length to 2.54 Å and a very weak binding to
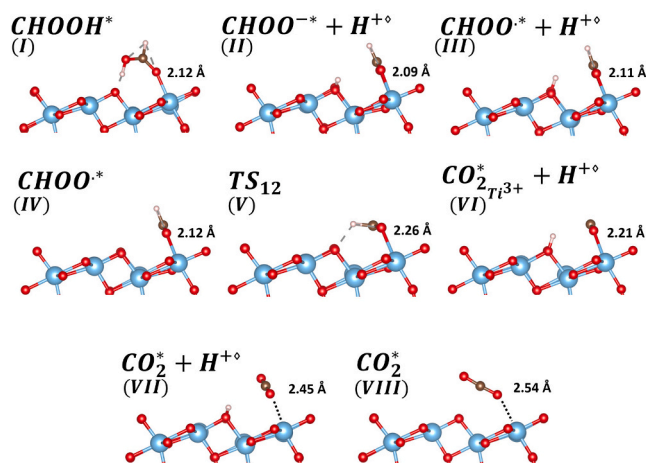

Fig. 7. Optimized geometries of surface species and transition states with characteristic bond lengths for the oxidation of CHOOH to CO_2 over the (101) anatase surface. Atoms are coloured as follows: O (red), Ti (blue), C (brown), H (light pink).

Table 1

List of elementary reaction steps that are embedded in the microkinetic model, along with the corresponding DFT-calculated rate coefficients (k), and expressions of the reaction rates. The symbols * and ◇ indicate the Ti and oxygen bridge active sites, respectively. ϑ_0 and φ_0 represent the fractional coverages of Ti_{5c}^{4+} and oxygen bridge vacant sites, respectively. ϑ_i and φ_i represent the fractional coverages of surface species i on the Ti_{5c}^{4+} and oxygen bridge sites, respectively. C_i represents the concentration of molecular species i in the reacting system. C_{h^+} and C_{e^-} indicate the concentrations of surface-reaching holes and electrons in monolayer.

Reaction #	Reaction	k (s^{-1})	Reaction rate expression
1	$CH_3OH + * \rightarrow CH_3OH^*$	$3.17 \cdot 10^{10}$	$r = kC_{CH_3OH}\vartheta_0$
2	$CH_3OH^* \rightarrow CH_3OH + *$	$7.48 \cdot 10^6$	$r = k\vartheta_{CH_3OH}$
3	$CH_3OH^* + \diamond \rightarrow CH_3O^{-*} + H^{+\diamond}$	$1.58 \cdot 10^6$	$r = k\vartheta_{CH_3OH}\varphi_0$
4	$CH_3O^{-*} + H^{+\diamond} \rightarrow CH_3OH^* + \diamond$	$5.61 \cdot 10^9$	$r = k\vartheta_{CH_3O^-}\,\varphi_{H^+}$
5	$CH_3OH^* + OH^{-*} \rightarrow CH_3O^{-*} + H_2O^*$	$8.86 \cdot 10^{11}$	$r = k\vartheta_{CH_3OH}\vartheta_{OH}$
6	$CH_3O^{-*} + H_2O^* \rightarrow CH_3OH^* + OH^{-*}$	$1.18 \cdot 10^{10}$	$r = k\vartheta_{CH_3O}\,\vartheta_{H_2O}$
7	$CH_3O^{-*} + h^+ \rightarrow CH_3O^\bullet$	$6.21 \cdot 10^{12}$	$r = k\vartheta_{CH_3O^-}\,C_{h^+}$
8	$CH_3O^{\bullet*} + \diamond \rightarrow CH_2O^*_{Ti^{3+}} + H^{+\diamond}$	$1.22 \cdot 10^{10}$	$r = k\vartheta_{CH_3O}\,\varphi_0$
9	$CH_2O^*_{Ti^{3+}} + h^+ \rightarrow CH_2O^*$	$6.21 \cdot 10^{12}$	$r = k\vartheta_{CH_2O_{Ti^{3+}}}\,C_{h^+}$
10	$CH_2O + * \rightarrow CH_2O^*$	$3.38 \cdot 10^{10}$	$r = kC_{CH_2O}\vartheta_0$
11	$CH_2O^* \rightarrow CH_2O + *$	$5.80 \cdot 10^{10}$	$r = k\vartheta_{CH_2O}$
12	$CH_2O^* + OH^{-*} \rightarrow CHO^{-*} + H_2O^*$	$6.21 \cdot 10^{12}$	$r = k\vartheta_{CH_2O}\vartheta_{OH}$
13	$CHO^{\bullet*} + \diamond \rightarrow CO^*_{Ti^{3+}} + H^{+\diamond}$	$1.93 \cdot 10^{12}$	$r = k\vartheta_{CHO}\,\varphi_0$
14	$CO^*_{Ti^{3+}} + h^+ \rightarrow CO^*$	$6.21 \cdot 10^{12}$	$r = k\vartheta_{CH_2O_{Ti^{3+}}}\,C_{h^+}$
15	$CO + * \rightarrow CO^*$	$3.62 \cdot 10^{10}$	$r = kC_{CO}\vartheta_0$
16	$CO^* \rightarrow CO + *$	$6.21 \cdot 10^{12}$	$r = k\vartheta_{CO}$
17	$H_2O + * \rightarrow H_2O^*$	$5.63 \cdot 10^{10}$	$r = kC_{H_2O}\vartheta_0$
18	$H_2O^* \rightarrow H_2O + *$	$1.10 \cdot 10^7$	$r = k\vartheta_{H_2O}$
19	$H_2O^* + \diamond \rightarrow OH^{-*} + H^{+\diamond}$	$3.32 \cdot 10^5$	$r = k\vartheta_{H_2O}\varphi_0$
20	$OH^{-*} + H^{+\diamond} \rightarrow H_2O^* + \diamond$	$2.76 \cdot 10^{11}$	$r = k\vartheta_{OH^-}\,\varphi_{H^+}$
21	$OH^{-*} + h^+ \rightarrow OH^{\bullet*}$	$6.21 \cdot 10^{12}$	$r = k\vartheta_{OH^-}\,C_{h^+}$
22	$OH^{\bullet*} + \diamond \rightarrow O^{-*} + H^{+\diamond}$	$4.28 \cdot 10^1$	$r = k\vartheta_{OH}\,\varphi_0$
23	$O^{-*} + H^{+\diamond} \rightarrow OH^{\bullet*} + \diamond$	$2.49 \cdot 10^8$	$r = k\vartheta_{O^-}\,\varphi_{H^+}$
24	$O^{-*} + h^+ \rightarrow O^*$	$6.21 \cdot 10^{12}$	$r = k\vartheta_{O_{Ti^{3+}}}\,C_{h^+}$
25	$O_2 + * + * \rightarrow O^* + O^*$	$3.17 \cdot 10^{10}$	$r = kC_{O_2}\vartheta_0^2$
26	$O^* + O^* \rightarrow O_2 + * + *$	$6.21 \cdot 10^{12}$	$r = k\vartheta_O^2$
27	$CHO^* + OH^* \rightarrow CHOOH^* + *$	$6.21 \cdot 10^{12}$	$r = k\vartheta_{CHO}\,\vartheta_{OH}$
28	$CH_2O^* + H_2O^* \rightarrow CH_2(OH)_2^* + *$	$6.11 \cdot 10^0$	$r = k\vartheta_{CH_2O}\vartheta_{H_2O}$
29	$CH_2(OH)_2^* + * \rightarrow CH_2O^* + H_2O^*$	$3.32 \cdot 10^5$	$r = k\vartheta_{CH_2(OH)_2}\vartheta_0$
30	$CH_2(OH)_2 + * \rightarrow CH_2(OH)_2^*$	$2.03 \cdot 10^{10}$	$r = kC_{CH_2(OH)_2}\vartheta_0$
31	$CH_2(OH)_2^* \rightarrow CH_2(OH)_2 + *$	$2.49 \cdot 10^8$	$r = k\vartheta_{CH_2(OH)_2}$
32	$CH_2(OH)_2^* + \diamond \rightarrow CH_2OOH^{-*} + H^{+\diamond}$	$3.80 \cdot 10^9$	$r = k\vartheta_{CH_2(OH)_2}\varphi_0$
33	$CH_2OOH^{-*} + H^{+\diamond} \rightarrow CH_2(OH)_2^* + \diamond$	$1.48 \cdot 10^4$	$r = k\vartheta_{CH_2OOH^-}\,\varphi_{H^+}$
34	$CH_2OOH^{-*} + h^+ \rightarrow CH_2OOH^{\bullet*}$	$6.21 \cdot 10^{12}$	$r = k\vartheta_{CH_2OOH^-}\,C_{h^+}$
35	$CH_2OOH^{\bullet*} + \diamond \rightarrow CHOOH^*_{Ti^{3+}} + H^{+\diamond}$	$9.98 \cdot 10^3$	$r = k\vartheta_{CH_2OOH}\,\varphi_0$
36	$CHOOH^*_{Ti^{3+}} + h^+ \rightarrow CHOOH^*$	$6.21 \cdot 10^{12}$	$r = k\vartheta_{CHOOH_{Ti^{3+}}}\,C_{h^+}$
37	$CHOOH + * \rightarrow CHOOH^*$	$2.20 \cdot 10^{10}$	$r = kC_{CHOOH}\vartheta_0$
38	$CHOOH^* \rightarrow CHOOH + *$	$4.07 \cdot 10^{11}$	$r = k\vartheta_{CHOOH}$
39	$CHOOH^* + \diamond \rightarrow CHOO^{-*} + H^{+\diamond}$	$6.21 \cdot 10^{12}$	$r = k\vartheta_{CHOOH}\varphi_0$
40	$CHOO^{-*} + H^{+\diamond} \rightarrow CHOOH^* + \diamond$	$4.07 \cdot 10^{11}$	$r = k\vartheta_{CHOO^-}\,\varphi_{H^+}$
41	$CHOO^{-*} + h^+ \rightarrow CHOO^*$	$6.21 \cdot 10^{12}$	$r = k\vartheta_{CHOO^-}\,C_{h^+}$
42	$CHOO^{-*} + \diamond \rightarrow CO_{2Ti^{3+}}^* + H^{+\diamond}$	$8.01 \cdot 10^8$	$r = k\vartheta_{CHOO}\,\varphi_0$
43	$CO_{2Ti^{3+}}^* + h^+ \rightarrow CO_2^*$	$6.21 \cdot 10^{12}$	$r = k\vartheta_{CO_{2Ti^{3+}}}\,C_{h^+}$
44	$CO_2 + * \rightarrow CO_2^*$	$2.30 \cdot 10^{10}$	$r = kC_{CO_2}\vartheta_0$
45	$CO_2^* \rightarrow CO_2 + *$	$8.86 \cdot 10^{11}$	$r = k\vartheta_{CO_2}$
46	$H^{+\diamond} + H^{+\diamond} + 2e^- \rightarrow H_2 + \diamond + \diamond$	$1.00 \cdot 10^{13}$	$r = k\varphi_{H^+}^2 \bullet C_{e^-}^2$

the surface, only 0.09 eV below gas-phase CO_2.

This detailed analysis of the mechanism of methanol oxidation highlights the complexity of the process, with two pathways available for methanol oxidation to formaldehyde (a photoinduced pathway and a hydroxyl-assisted pathway), and two possible follow-up oxidation pathways: hydroxyl-assisted oxidation of formaldehyde to carbon monoxide and water-assisted oxidation of formaldehyde to CO_2. In particular, the latter two pathways differ in the number of photo-holes required to complete the process and in the nature of the final oxidation product. While the data on the reaction mechanisms and energy barriers can be used to assess the thermodynamic and kinetic favourability of these pathways and expected products and intermediates, they do not provide information on the amounts of products and intermediates formed in this complex photocatalytic process. To obtain quantitative insight into the prevalence of various products, the information on reaction steps based on the DFT modelling have been combined with microkinetic modelling in the second step of this study.

3.2. Microkinetic model

Table 1 provides an overview of all elementary reaction steps incorporated in the microkinetic model, along with the corresponding DFT-calculated rate coefficients (k) and expressions of the reaction rates. These reaction steps describe the mechanistic pathway of methanol reforming into C_1 products and water splitting, with simultaneous formation of O_2 and H_2. The symbols * and ◇ indicate the Ti_{5c}^{4+} and oxygen bridge active sites, respectively. ϑ_0 and φ_0 represent the fractional coverages of Ti_{5c}^{4+} and oxygen bridge vacant sites, respectively. ϑ_i and φ_i represent the fractional coverages of surface species i on the Ti_{5c}^{4+} and oxygen bridge sites, respectively. C_i represents the concentration of molecular species i in the reacting system with respect to the standard state concentration (1 mol·L^{-1}). C_{h^+} and C_{e^-} indicate the concentrations of surface-reaching holes and electrons in monolayer. In Table 1, the generic kinetic expressions for the adsorption (ads) and desorption (des) of species i as well as for surface (surf) reactions, are expressed as follows:

$$r_{ads} = k_{ads}C_i\vartheta_0 \tag{8}$$

$$r_{des} = k_{des}\vartheta_i \tag{9}$$

$$r_{surf} = k_{surf}\prod\vartheta_i \tag{10}$$

with specific reference to the Ti_{5c}^{4+} sites. In reactions involving charge carriers, the concentrations of photogenerated electrons or holes are explicitly included in the rate expression.

The critical role of charge recombination in determining photocatalytic performance of metal-loaded semiconductors is extensively reported in the literature [106] [107] [108]. In our previous work [46], photoluminescence spectroscopy revealed that surface modification of anatase with different noble metals effectively suppressed electron-hole recombination, following the trend Pt > Pd ≈ Au > Ag under UV and visible light irradiation. On the other hand, no clear correlation was observed between nanoparticle size/dispersion and hydrogen evolution rates, indicating that these parameters are not the primary factors controlling photocatalytic efficiency. Wang et al. estimated the concentration of surface-reaching holes of ≈ 1 • 10^{-9} (monolayers) for pristine TiO$_2$ [109] based on a study by Thompson and Yates [110] where TiO$_2$ was irradiated by UV light (365 nm), matching the dominant emission wavelength of the lamp used in the present study. Variations in photon flux could change the concentration of holes and electrons reaching the catalyst surface [111] [112] [113]. Such variations can be incorporated in the model by adjusting the concentration of charge carriers. For instance, a higher concentration of surface charges would enhance the generation of surface radical species, thereby promoting the oxidation pathways and ultimately increasing the overall hydrogen production. The concentrations of surface reaching holes for the metal loaded TiO$_2$ were estimated (Table S3) by scaling this value with respect to the intensity of the photoluminescence spectra reported in [46].

To evaluate the energy change associated with the migration of an adsorbed proton from the O$_{br}$ site to a metal site, we constructed a trimer

Table 2

DFT-calculated and estimated rate coefficients and equilibrium constants with their 95 % confidence intervals for key elementary steps included in the reaction network. Reaction 46 is irreversible and therefore has no associated K_{eq} value.

Reaction #	Reaction	DFT calculated rate coefficient		Estimated rate coefficient	
		k (s^{-1})	K_{eq}	k (s^{-1})	K_{eq}
1 & 2	$CH_3OH + {}^* \leftrightarrow CH_3OH^*$	$3.17 \cdot 10^{10}$	$4.24 \cdot 10^3$	$(3.50 \pm 0.34) \cdot 10^{10}$	$(1.58 \pm 0.25) \cdot 10^3$
3 & 4	$CH_3OH^* + \diamond \leftrightarrow CH_3O^{-*} + H^{+\diamond}$	$1.58 \cdot 10^6$	$2.81 \cdot 10^{-4}$	$1.58 \cdot 10^6$ *	$(3.69 \pm 0.91) \cdot 10^{-5}$
5 & 6	$CH_3OH^* + OH^* \leftrightarrow CH_3O^{-*} + H_2O^*$	$8.86 \cdot 10^{11}$	$7.54 \cdot 10^1$	$(3.69 \pm 0.17) \cdot 10^{12}$	$(2.26 \pm 0.52) \cdot 10^1$
17 & 18	$H_2O + {}^* \leftrightarrow H_2O^*$	$5.63 \cdot 10^{10}$	$5.10 \cdot 10^3$	$(3.74 \pm 0.82) \cdot 10^{10}$	$(4.51 \pm 0.42) \cdot 10^3$
19 & 20	$H_2O^* + \diamond \leftrightarrow OH^{-*} + H^{+\diamond}$	$3.32 \cdot 10^5$	$1.21 \cdot 10^{-6}$	$3.32 \cdot 10^5$ *	$(3.32 \pm 0.83) \cdot 10^{-8}$
22 & 23	$OH^{\bullet*} + \diamond \leftrightarrow O^{-*} + H^{+\diamond}$	$4.28 \cdot 10^1$	$1.72 \cdot 10^{-7}$	$4.28 \cdot 10^1$ *	$(1.20 \pm 0.22) \cdot 10^{-6}$
46	$H^{+\diamond} + H^{+\diamond} + 2e^- \to H_2 + {}^* + \diamond$	$1.00 \cdot 10^{13}$	–	$(1.54 \pm 0.13) \cdot 10^{13}$	–

* Rate coefficients not included in the estimation procedure.

metal cluster on anatase as described in our previous work [46]. In all cases, the transfer of a proton from the O_{br} to a metal site was found to be energetically favourable with a downhill energy profile as depicted in Table S4. For this reason, the migration of the proton from the oxygen bridge to the photodeposited metal cluster was assumed to occur as a barrierless process without an energy penalty. As a result, and in consensus with other kinetic models [114] [115], hydrogen recombination was considered to occur exclusively on the transition metal sites, with H_2 formation fast and irreversible ($k = 10^{13}$ s^{-1}).

To assess the change in Gibbs free energy of adsorption when multiple molecules adsorb onto the catalyst surface, we analysed the coverage-dependent adsorption configurations of methanol and water across a coverage range of 0.25 to 1 ML, where 1 ML is defined as one molecule per surface Ti_{5c} atom. Fig. S9 presents the coverage-dependent Gibbs free energies of adsorption for methanol and water. This analysis indicates that, on a fully covered TiO_2 surface, the adsorption free energy decreases by approximately 34 % for methanol and by 29 % for water compared to the adsorption on an empty surface. Accordingly, to reflect the fully covered state of the catalyst, all desorption barriers included in the model were reduced by 34 % with respect to the values calculated for the adsorption on an empty surface, with the exception for water, whose desorption barrier was reduced by 29 %.

The reaction rates listed in Table 1 were incorporated into the design

equation of an ideal batch reactor to simulate the results of the experimental procedures. The resulting mathematical model consisted of 46 differential equations describing the change in concentration (or surface coverage) of each molecular (or surface) species, and two algebraic equations describing the material balances on the active sites. These were expressed according to eqs. (11) and (12) for the Ti_{5c}^{4+} and O_{br} active sites, respectively.

$$\sum \vartheta_i + \vartheta_0 = 1 \tag{11}$$

$$\varphi_H + \varphi_0 = 1 \tag{12}$$

The total number of active sites was calculated based on a Ti_{5c}^{4+} site density of $5.17 \cdot 10^{14}$ sites cm^{-2} [116], and an anatase specific surface area of 100 m^2 g^{-1} [117].

The reaction rate constants, as derived from transition state theory, were used to describe the kinetics of the process. Key rate coefficients listed in Table 2 were adjusted within 2 orders of magnitude. These adjustments reflect the intrinsic uncertainty associated with DFT calculations at the GGA level, which typically exhibit an error margin of approximately 20 kJ mol^{-1} [118], and the effect of structural inhomogeneities, such as minority facets [78] and surface defects [119] on the anatase surface, on the reaction barriers.

The model was integrated using the DDASAC solver [120], while parameter estimation was conducted with a gradient-based local optimizer (GREG) [121]. This estimation aimed to minimize an objective function defined as the sum of the squared errors between experimental and calculated hydrogen productions. Table 2 lists the values of the rate coefficients included in the estimation procedure together with their DFT-calculated values.

Fig. 8 shows a comparison of experimental and calculated hydrogen production over anatase loaded with Pd, Ag, Pt, and Au, and the best fit of the microkinetic model. The amount of hydrogen produced increases with methanol concentration in the range 0.0–3.0 M. At low methanol concentrations the reaction kinetics are limited by the surface availability of methanol molecules, as indicated by the increase in hydrogen production rate. As methanol concentration increases, hydrogen production gradually reaches a plateau. Among the investigated cocatalysts, Pt exhibits the highest activity in terms of hydrogen evolution, while Ag shows the lowest performance. Under UV/visible light irradiation, the trend in hydrogen production follows the order Pt > Pd ≈ Au > Ag, reflecting the differences in the charge carrier recombination rates experimentally revealed from photoluminescence spectroscopy [46].

The proposed model can accurately (mean absolute error of 1.34 • 10^{-3} mol L^{-1}) capture the hydrogen production rate as a function of the concentration of methanol.

The simulated methanol and water surface coverages on metal-loaded anatase collectively account for over 99 % of the total catalyst coverage. Comparable surface coverage trends were observed across all metal-loaded catalysts, with no significant differences between them.
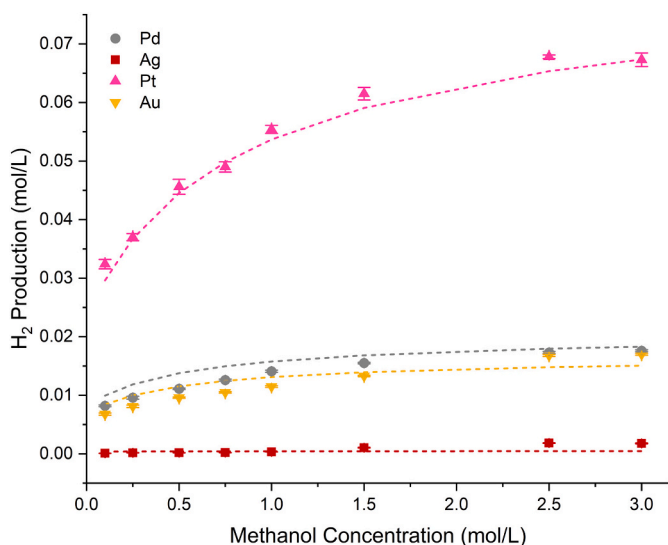

Fig. 8. H_2 production from methanol reforming over anatase loaded with Pd (grey), Ag (red), Pt (pink), and Au (gold) at 2 h of reaction time as a function of methanol concentration. Symbols and dashed lines represent experimental and simulated hydrogen productions, respectively. Experimental conditions: Catalyst load = 500 ppm, neutral pH, T = 298 K, UV and visible light irradiation.
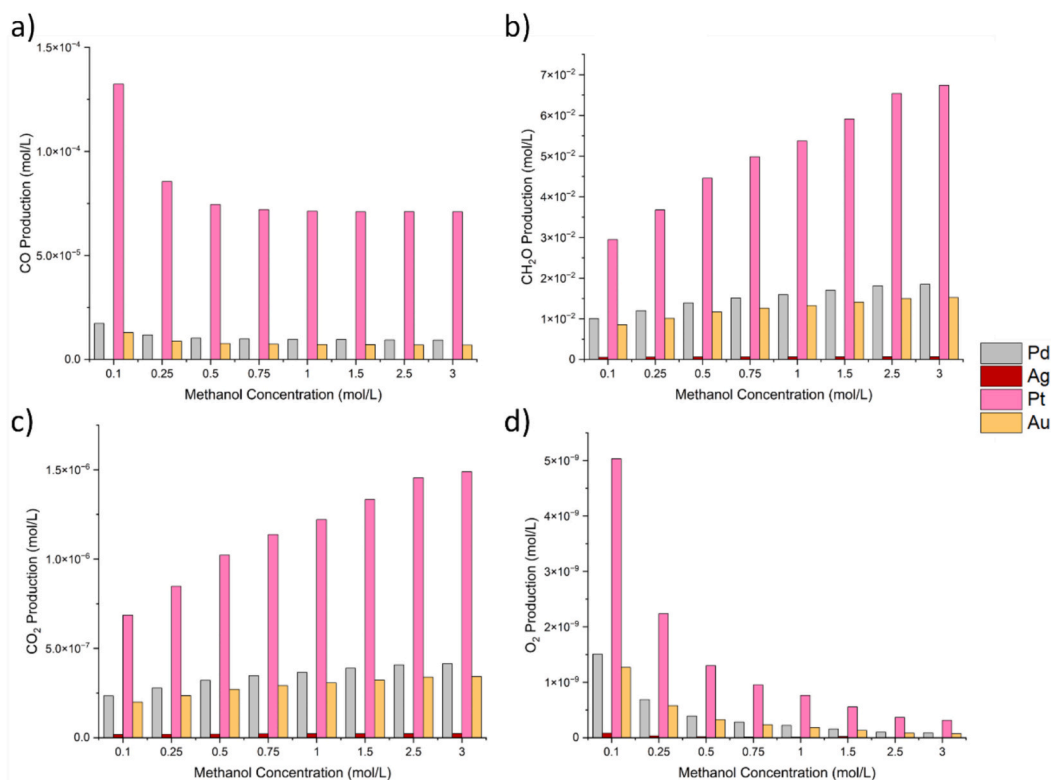
Fig. 9. Simulated CO (a) CH$_2$O (b), CO$_2$ (c) and O$_2$ (d) production from methanol reforming over anatase loaded with Pd (grey), Ag (red), Pt (pink), and Au (gold) at 2 h of reaction time.
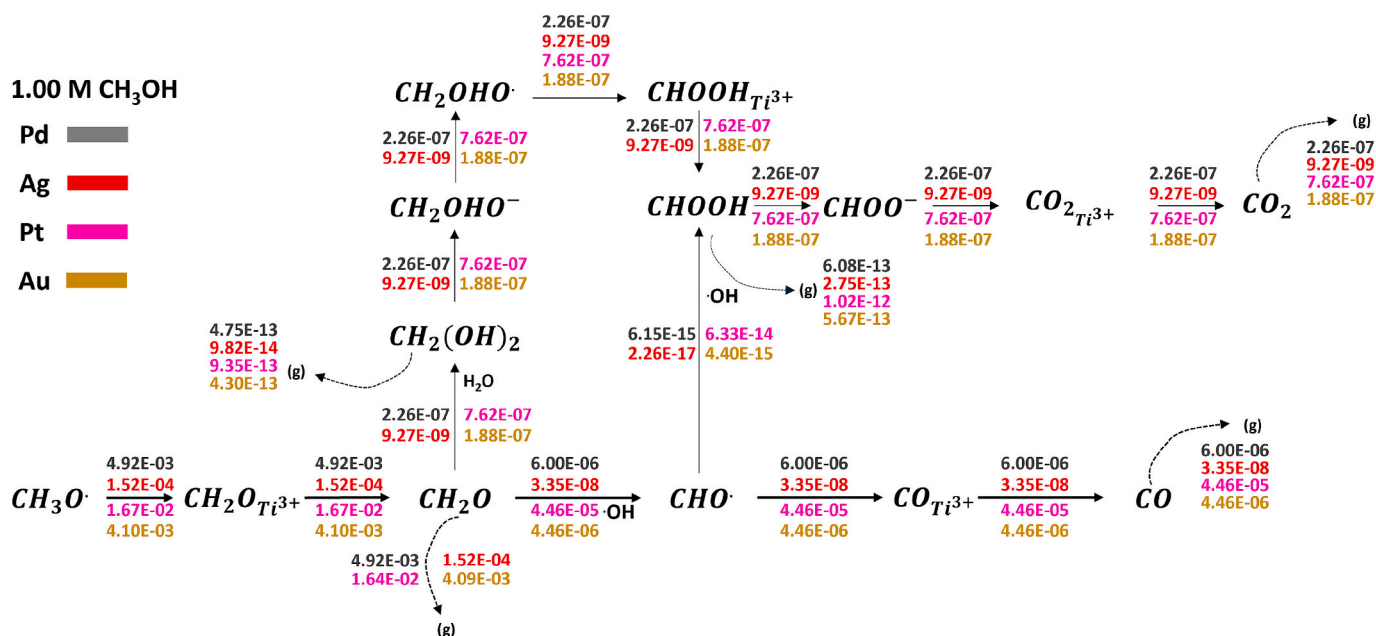

Fig. 10. Net-rate analysis for the photoreforming of methoxy radical into CO$_2$ or CO over Pd (grey), Ag (red), Pt (pink), and Au (gold) on TiO$_2$ at a concentration of methanol of 1.00 M and at 2 h of reaction time. The net rate values have units s^{-1}. The arrows for adsorption/desorption (curved) and surface reactions (straight) are directed towards the species with a positive rate of formation. (g) indicates the species in the gas phase.

The production of CO (Fig. 9a) decreases before reaching a plateau with increasing methanol concentration. In contrast, CH$_2$O (Fig. 9b) and CO$_2$ (Fig. 9c) exhibit similar behaviour to H$_2$ production with increasing methanol concentration. Fig. 9d shows that increasing methanol concentration results in a sharp decrease in O$_2$ production. This effect is two-fold: first, the decreased H$_2$O surface coverage reduces the rate of dehydrogenation reactions that generate hydroxyl anions; second, the increased methanol coverage results in the formation of more transient

methanol-derived products which consume additional hydroxyl radicals. This means that fewer hydroxyl radicals overcome the activation barrier to form oxygen radicals, reducing the overall amount of molecular oxygen produced.

A net-rate analysis of a segment of the reaction network illustrating the oxidation of the methoxy radical to CO and CO$_2$ is presented in Fig. 10. The arrows in the network point to species with a positive rate of formation, with the net-rates expressed in s^{-1}. The primary reaction

pathway involves the partial oxidation of methanol to CO proceeding through the intermediate formation of formaldehyde. CO_2 is predominantly produced from the oxidation of formic acid, which originates from the hydration of formaldehyde. However, the overall CO_2 yield remains low due to the kinetic limitations of this pathway. The hydration of formaldehyde is considerably less kinetically favourable than its partial oxidation to the formyl radical. Surface hydroxyl radicals are primarily consumed through the interaction with formaldehyde, leading to the formation of the formyl radical. However, the desorption of formaldehyde along with the low concentration of surface hydroxyls results in low production of CO.

4. Conclusion

This work presents a comprehensive investigation of the mechanism of methanol reforming and the construction of a microkinetic model to describe the kinetics of hydrogen production via methanol photo-reforming on metal loaded anatase at a mechanistic level. A reaction network was developed to map the photoreforming process forming C_1 products with no a priori assumptions on the rate determining steps. The rate coefficients governing the process were estimated based on DFT calculations and transition state theory. Our DFT calculations show that the photoreforming of methanol to carbon monoxide is thermodynamically and kinetically accessible. By comparison, hydrogen production from water is less accessible, because the splitting of the OH radical is unfavourable due to its high barrier (0.66 eV) and significantly endothermic nature, which can be attributed to the small size of the oxygen anion and its limited ability to delocalise the negative charge. However, synergistic pathways involving formaldehyde and its intermediates, in combination with surface hydroxyl species, offer kinetically favourable routes for hydrogen production. The microkinetic model simulations were validated using experiments conducted under UV and visible light irradiation, revealing a hydrogen production trend that follows the order Pt > Pd ≈ Au > Ag. The microkinetic analysis provides detailed mechanistic insights into the reaction kinetics with some minor optimisation to take into account the different kinetics of other anatase facets. Surface hydroxyl radicals are primarily consumed through their reaction with formaldehyde, highlighting the crucial synergy between water and methanol oxidation pathways. As a result, the production of formic acid and its subsequent conversion to CO_2 is minimal. Similarly, the formation of methanediol in the reacting system is negligible. This work marks the first application of microkinetic modelling to photocatalytic hydrogen evolution, demonstrating strong predictive capabilities and highlighting key factors governing catalyst performance. These findings lay the groundwork for using microkinetic methods to design more efficient photocatalysts, while contributing to advancing sustainable hydrogen production and solar energy conversion technologies.

CRediT authorship contribution statement

Matthew J. Wigglesworth: Writing – original draft, Investigation, Formal analysis, Data curation. **Ruiman Ma:** Writing – original draft, Methodology, Investigation, Data curation. **Natalia Martsinovich:** Writing – review & editing, Supervision, Conceptualization. **Sergio Vernuccio:** Writing – review & editing, Supervision, Funding acquisition, Conceptualization.

Declaration of competing interest

The authors declare that they have no known competing financial interests or personal relationships that could have appeared to influence the work reported in this paper.

Acknowledgments

Appendix A. Supplementary data

Supplementary data to this article can be found online at https://doi.org/10.1016/j.cej.2025.168334.

Data availability

Data will be made available on request.

References

[1] A. Fujishima, K. Honda, Electrochemical photolysis of water at a semiconductor electrode, Nature 238 (5358) (1972) 37–38, https://doi.org/10.1038/238037a0.

[2] S.B. Beil, S. Bonnet, C. Casadevall, R.J. Detz, F. Eisenreich, S.D. Glover, Christoph Kerzig, Line Næsborg, S. Pullen, G. Storch, N. Wei, C. Zeymer, Challenges and future perspectives in Photocatalysis: conclusions from an interdisciplinary workshop, JACS Au 4 (8) (2024) 2746–2766, https://doi.org/10.1021/jacsau.4c00527.

[3] Y. Chen, L. Soler, C. Cazorla, J. Oliveras, N.G. Bastús, V.F. Puntes, J. Llorca, Facet-engineered TiO2 drives photocatalytic activity and stability of supported noble metal clusters during H2 evolution, Nat. Commun. 14 (1) (2023) 6165, https://doi.org/10.1038/s41467-023-41976-2.

[4] H. Zhao, L. Jian, M. Gong, M. Jing, H. Li, Q. Mao, T. Lu, Y. Guo, R. Ji, W. Chi, Y. Dong, Y. Zhu, Transition-metal-based Cocatalysts for photocatalytic water splitting, Small Struct. 3 (7) (2022) 2100229, https://doi.org/10.1002/sstr.202100229.

[5] X. Li, L. Chen, J. Wang, J. Zhang, C. Zhao, H. Lin, Y. Wu, Y. He, Novel platinum-bismuth alloy loaded KTa0.5Nb0.5O3 composite photocatalyst for effective nitrogen-to-ammonium conversion, J. Colloid Interface Sci. 618 (2022) 362–374, https://doi.org/10.1016/j.jcis.2022.03.096.

[6] L. Cheng, P. Zhang, Q. Wen, J. Fan, Q. Xiang, Copper and platinum dual-single-atoms supported on crystalline graphitic carbon nitride for enhanced photocatalytic CO2 reduction, Chin. J. Catal. 43 (2) (2022) 451–460, https://doi.org/10.1016/s1872-2067(21)63879-2.

[7] Y. Li, S. Li, H. Huang, Metal-enhanced strategies for photocatalytic and photoelectrochemical CO2 reduction, Chem. Eng. J. 457 (2022) 141179, https://doi.org/10.1016/j.cej.2022.141179.

[8] J. Fu, Q. Xu, J. Low, C. Jiang, J. Yu, Ultrathin 2D/2D WO3/g-C3N4 step-scheme H2-production photocatalyst, Appl. Catal. B Environ. 243 (2019) 556–565, https://doi.org/10.1016/j.apcatb.2018.11.011.

[9] J. Wang, Y. Shi, H. Sun, W. Shi, F. Guo, Fabrication of Bi4Ti3O12/ZnIn2S4 S-scheme heterojunction for achieving efficient photocatalytic hydrogen production, J. Alloys Compd. 930 (2022) 167450, https://doi.org/10.1016/j.jallcom.2022.167450.

[10] Z. Xie, L. Xie, F. Qi, H. Liu, L. Meng, J. Wang, Y. Xie, J. Chen, C.-Z. Lu, Efficient photocatalytic hydrogen production by space separation of photo-generated charges from S-scheme ZnIn2S4/ZnO heterojunction, J. Colloid Interface Sci. 650 (2023) 784–797, https://doi.org/10.1016/j.jcis.2023.07.032.

[11] J. Zhang, Y. Zhao, K. Qi, S. Liu, CuInS2 quantum-dot-modified g-C3N4 S-scheme heterojunction photocatalyst for hydrogen production and tetracycline degradation, J. Mater. Sci. Technol. 172 (2023) 145–155, https://doi.org/10.1016/j.jmst.2023.06.042.

[12] Z. Jin, C. Yang, L. Li, J. Jiang, Rational constructing 2D/3D p-n heterojunctions to modulate hydrogen evolution efficient pathways for enhances photocatalytic hydrogen production, J. Ind. Eng. Chem. 142 (2025) 449–462, https://doi.org/10.1016/j.jiec.2024.07.052.

[13] X. Kong, K. Wang, Z. Jin, Enhanced photocatalytic hydrogen production through p-n heterojunction interface engineering using Prussian blue analogue-derived co–cu–P with graphdiyne (g-CnH2n-2) crystalline/amorphous, Int. J. Hydrog. Energy 98 (2024) 170–183, https://doi.org/10.1016/j.ijhydene.2024.12.036.

[14] X. Li, Y. Li, P. Zhu, Z. Jin, Integrating Co3O4 with ZnIn2S4 p-n heterojunction for efficient photocatalytic hydrogen production, Int. J. Energy Res. 46 (11) (2022) 15589–15601, https://doi.org/10.1002/er.8254.

[15] Y. Zhang, Z. Lu, H. Chen, X. Kang, P. Wang, Z. Xian, Z. Zhang, Y. Cai, G. Lu, Encapsulation of Pt/TiO2@MoS2+x with polymethyl methacrylate for enhancement of photocatalytic hydrogen evolution in seawater, Chem. Eng. J. (2025) 163378, https://doi.org/10.1016/j.cej.2025.163378.

[16] A. Khan, M.L. Pivert, Alireza Ranjbari, D. Dragoe, D. Bahena-Uribe, Christophe Colbeau-Justin, C. Herrero, Dorota Rutkowska-Zbik, J. Deschamps, Hynd Remita, Cu-based MOF/TiO2 composite nanomaterials for photocatalytic

hydrogen generation and the role of copper, Adv. Funct. Mater. (2025), https://doi.org/10.1002/adfm.202501736.

[17] X. Li, X. Feng, D. Meng, X.-J. Hu, L. Li, Y. Zhang, X. Wang, Fabrication of TiO₂/MOF type II heterojunction by growth of TiO₂ on Cr-based MOF for enhanced photocatalytic hydrogen production, Cryst. Growth Des. (2025), https://doi.org/10.1021/acs.cgd.4c01530.

[18] Y. Lu, B. Jaeckel, B.A. Parkinson, Preparation and characterization of terraced surfaces of low-index faces of anatase, rutile, and brookite, Langmuir : the ACS journal of surfaces and colloids 22 (10) (2006) 4472–4475, https://doi.org/10.1021/la053509m.

[19] Y. Yamamoto, K. Nakajima, Takeo Ohsawa, Y. Matsumoto, Hideomi Koinuma, Preparation of atomically smooth TiO2 single crystal surfaces and their photochemical property, Jpn. J. Appl. Phys. 44 (4L) (2005) L511, https://doi.org/10.1143/jjap.44.l511.

[20] C. Arrouvel, Mathieu Digne, M. Breysse, Hervé Toulhoat, Pascal Raybaud, Effects of morphology on surface hydroxyl concentration: a DFT comparison of anatase–TiO2 and γ-alumina catalytic supports, J. Catal. 222 (1) (2004) 152–166, https://doi.org/10.1016/j.jcat.2003.10.016.

[21] T. Luttrell, S. Halpegamage, J. Tao, A. Kramer, E. Sutter, M. Batzill, Why is anatase a better photocatalyst than rutile? - model studies on epitaxial TiO2 films, Sci. Rep. 4 (1) (2014), https://doi.org/10.1038/srep04043.

[22] U. Diebold, The surface science of titanium dioxide, Surf. Sci. Rep. 48 (5–8) (2003) 53–229, https://doi.org/10.1016/s0167-5729(02)00100-0.

[23] A. Fujishima, T.N. Rao, D.A. Tryk, Titanium dioxide photocatalysis, J. Photochem. Photobiol. C Photchem. Rev. 1 (1) (2000) 1–21, https://doi.org/10.1016/s1389-5567(00)00002-2.

[24] H. Hussain, G. Tocci, T. Woolcot, X. Torrelles, C.L. Pang, D.S. Humphrey, C. M. Yim, D.C. Grinter, G. Cabailh, O. Bikondoa, R. Lindsay, J. Zegenhagen, A. Michaelides, G. Thornton, Structure of a model TiO2 photocatalytic interface, Nat. Mater. 16 (4) (2016) 461–466, https://doi.org/10.1038/nmat4793.

[25] P. Jiménez-Calvo, V. Caps, V. Keller, Plasmonic au-based junctions onto TiO2, gC3N4, and TiO2-gC3N4 systems for photocatalytic hydrogen production: fundamentals and challenges, Renew. Sust. Energ. Rev. 149 (2021) 111095, https://doi.org/10.1016/j.rser.2021.111095.

[26] M. Bowker, C. Morton, J. Kennedy, H. Bahruji, J. Greves, W. Jones, P.R. Davies, C. Brookes, P.P. Wells, N. Dimitratos, Hydrogen production by photoreforming of biofuels using au, Pd and au–Pd/TiO2 photocatalysts, J. Catal. 310 (2014) 10–15, https://doi.org/10.1016/j.jcat.2013.04.005.

[27] J. Tang, J.R. Durrant, D.R. Klug, Mechanism of photocatalytic water splitting in TiO2. Reaction of water with Photoholes, importance of charge carrier dynamics, and evidence for four-hole chemistry, J. Am. Chem. Soc. 130 (42) (2008) 13885–13891, https://doi.org/10.1021/ja8034637.

[28] S.M. Thabet, Hani Nasser Abdelhamid, S.A. Ibrahim, H.M. El-Bery, Boosting photocatalytic water splitting of TiO2 using metal (Ru, Co, or Ni) co-catalysts for hydrogen generation, Sci. Rep. 14 (1) (2024), https://doi.org/10.1038/s41598-024-59608-0.

[29] R. Li, Y. Weng, X. Zhou, X. Wang, Y. Mi, R. Chong, H. Han, C. Li, Achieving overall water splitting using titanium dioxide-based photocatalysts of different phases, Energy Environ. Sci. 8 (8) (2015) 2377–2382, https://doi.org/10.1039/c5ee01398d.

[30] H. Eidsvåg, S. Bentouba, P. Vajeeston, S. Yohi, D. Velauthapillai, TiO2 as a photocatalyst for water splitting—an experimental and theoretical review, Molecules 26 (6) (2021) 1687, https://doi.org/10.3390/molecules26061687.

[31] J. Liu, Y. Wan, Y. Xie, F. Dong, K. Yang, X. Li, Boosting photocatalytic overall water splitting by β-NiS/TiO2-x Ohmic junction, Applied Catalysis B: Environment and Energy 379 (2025) 125690, https://doi.org/10.1016/j.apcatb.2025.125690.

[32] Y. Zhu, J. Ren, G. Huang, C. Dong, Y. Huang, P. Lu, H. Tang, Y. Liu, S. Shen, D. Yang, Red phosphorus grafted high-index (116) faceted anatase TiO2 for Z-scheme photocatalytic pure water splitting, Adv. Funct. Mater. 34 (9) (2023), https://doi.org/10.1002/adfm.202311623.

[33] X. Zhou, D. Chen, T. Li, X. Chen, L. Zhu, Pd and carbon quantum dots co-decorated TiO2 nanosheets for enhanced photocatalytic H2 production and reaction mechanism, Int. J. Hydrog. Energy 53 (2024) 1361–1372, https://doi.org/10.1016/j.ijhydene.2023.12.004.

[34] S.S. Rayalu, D. Jose, M.V. Joshi, P.A. Mangrulkar, K. Shrestha, K. Klabunde, Photocatalytic water splitting on au/TiO2 nanocomposites synthesized through various routes: enhancement in photocatalytic activity due to SPR effect, Appl. Catal. B Environ. 142-143 (2013) 684–693, https://doi.org/10.1016/j.apcatb.2013.05.057.

[35] F. Guzman . Steven, C. Yang, Role of methanol sacrificing reagent in the photocatalytic evolution of hydrogen, Ind. Eng. Chem. Res. 52 (1) (2012) 61–65, https://doi.org/10.1021/ie301177s.

[36] S. Xia, T. Wang, Z. Ren, X. Yang, Q. Guo, C. Zhou, Adsorption structure–activity correlation in the photocatalytic chemistry of methanol and water on TiO2 (110), Acc. Chem. Res. (2024), https://doi.org/10.1021/acs.accounts.4c00578.

[37] H. Mao, Y. Tan, Q. Chen, M. Cai, C. Xu, T. Yang, Q. Gao, S. Zhang, Y. Fang, S. Liu, F. Peng, S. Yang, Synergistic photocatalytic CO₂ reduction and methanol oxidation via self-Photogenerated oxygen vacancy-rich TiO2 nanostructures, ACS Applied Nano Materials 7 (11) (2024) 12935–12943, https://doi.org/10.1021/acsanm.4c01281.

[38] H. Wang, H. Qi, X. Sun, S. Jia, X. Li, T.J. Miao, L. Xiong, S. Wang, X. Zhang, X. Liu, A. Wang, T. Zhang, W. Huang, J. Tang, High quantum efficiency of hydrogen production from methanol aqueous solution with PtCu–TiO2 photocatalysts, Nat. Mater. 22 (5) (2023) 619–626, https://doi.org/10.1038/s41563-023-01519-y.

[39] F. Zhao, Q. Bai, C. Xia, J. Hao, M. Gayot, J.-P. Delville, M.-H. Delville, Core–shell nanoheterodimers: laser-assisted deposition of single bimetallic au@M (M = au, ag, Pd, Pt) nanodots on TiO2 nanoparticles, Materials Advances 4 (2) (2023) 694–708, https://doi.org/10.1039/d2ma01018f.

[40] H. Šalipur, D. Lončarević, J. Dostanić, B. Likozar, A. Prašnikar, D. Manojlović, Nickel-loaded nitrogen-doped titanate nanostructured catalysts for solar-light driven hydrogen evolution and environmental remediation, Int. J. Hydrog. Energy 47 (26) (2022) 12937–12952, https://doi.org/10.1016/j.ijhydene.2022.02.054.

[41] S. Lv, M. Pei, Y. Liu, Z. Si, X. Wu, R. Ran, D. Weng, F. Kang, An isolation strategy to anchor atomic Ni or co cocatalysts on TiO2(A) for photocatalytic hydrogen production, Nano Res 15 (7) (2022) 5848–5856, https://doi.org/10.1007/s12274-022-4217-6.

[42] Muhammad Altaf Nazir, T. Najam, M. Altaf, K. Ahmad, I. Hossain, Mohammed Ali Assiri, Muhammad Sufyan Javed, Aziz ur Rehman, A. Shah, Tuning the photocatalytic hydrogen production via co-catalyst engineering, J. Alloys Compd. 990 (2024) 174378, https://doi.org/10.1016/j.jallcom.2024.174378.

[43] A. Meng, J. Zhang, D. Xu, J. Yu, J. Yu, Enhanced photocatalytic H 2 -production activity of anatase TiO 2 nanosheet by selectively depositing dual-cocatalysts on {101} and {001} facets, Appl. Catal. B Environ. 198 (2016) 286–294, https://doi.org/10.1016/j.apcatb.2016.05.074.

[44] M. Eder, C. Courtois, P. Petzoldt, S. Mackewicz, M. Tschurl, Ueli Heiz, Size and coverage effects of Ni and Pt co-catalysts in the photocatalytic hydrogen evolution from methanol on TiO2(110), ACS Catal. 12 (15) (2022) 9579–9588, https://doi.org/10.1021/acscatal.2c02230.

[45] S. Qin, J. Will, H. Kim, N. Denisov, S. Carl, E. Spiecker, Patrik Schmuki, Single atoms in Photocatalysis: Low loading is good enough!, ACS Energy Lett. 8 (2) (2023) 1209–1214, https://doi.org/10.1021/acsenergylett.2c02801.

[46] S. Hamdan, M.J. Wigglesworth, M. Muscetta, R. Ma, M.I. Helal, N. Martsinovich, G. Palmisano, S. Vernuccio, Unravelling the photoactivity of metal-loaded TiO2 for hydrogen production: insights from a combined experimental and computational analysis, Int. J. Hydrog. Energy 118 (2025) 394–406, https://doi.org/10.1016/j.ijhydene.2025.03.184.

[47] X. Ma, Y. Shi, J. Liu, X. Li, X. Cui, S. Tan, J. Zhao, B. Wang, Hydrogen-bond network promotes water splitting on the TiO2 surface, J. Am. Chem. Soc. 144 (30) (2022) 13565–13573, https://doi.org/10.1021/jacs.2c03690.

[48] C. Daldossi, C. Di Valentin, A. Selloni, Pathways of photocatalytic oxidation of formic acid on dry and hydrated Anatase TiO₂ surfaces, ACS Catal. 15 (13) (2025) 11487–11501, https://doi.org/10.1021/acscatal.5c01848.

[49] Naman Kumar Bharti, B. Modak, Enhancement of Photoactivity of TiO2 for potential applications in CO2 conversion and water splitting: A hybrid density functional theory study, J. Phys. Chem. C 126 (36) (2022) 15080–15093, https://doi.org/10.1021/acs.jpcc.2c03993.

[50] M. Setvin, X. Shi, J. Hulva, T. Simschitz, G.S. Parkinson, M. Schmid, C. D. Valentin, Annabella Selloni, U. Diebold, Methanol on Anatase TiO2 (101): mechanistic insights into Photocatalysis, ACS Catal. 7 (10) (2017) 7081–7091, https://doi.org/10.1021/acscatal.7b02003.

[51] H. Huang, J. Feng, S. Zhang, H. Zhang, X. Wang, T. Yu, C. Chen, Z. Yi, J. Ye, Z. Li, Z. Zou, Molecular-level understanding of the deactivation pathways during methanol photo-reforming on Pt-decorated TiO2, Appl. Catal. B Environ. 272 (2020) 118980, https://doi.org/10.1016/j.apcatb.2020.118980.

[52] F. Wu, Du, Sijia Lv, C. Zhao, X. Yang, DFT modeling of CO2 adsorption and HCOO● group conversion in Anatase au-TiO2-based Photocatalysis, ACS Omega 7 (8) (2022) 7179–7189, https://doi.org/10.1021/acsomega.1c06861.

[53] Vaidish Sumaria, T.B. Rawal, Y.F. Li, D. Sommer, J. Vikoren, R.J. Bondi, M. Rupp, A. Prasad, D. Prasad, Machine learning, density functional theory, and experiments to understand the photocatalytic reduction of CO2 on CuPt/TiO2, J. Phys. Chem. C 128 (34) (2024) 14247–14258, https://doi.org/10.1021/acs.jpcc.4c02275.

[54] R. Liu, X. Zhou, F. Yang, Y. Yu, Combination study of DFT calculation and experiment for photocatalytic properties of S-doped anatase TiO2, Appl. Surf. Sci. 319 (2014) 50–59, https://doi.org/10.1016/j.apsusc.2014.07.132.

[55] X. Tang, Qian Li Xue, X. Qi, C. Cheng, M. Yang, T. Yang, F. Chen, F. Qiu, X. Quan, DFT and experimental study on visible-light driven photocatalysis of rare-earth-doped TiO2, Vacuum 200 (2022) 110972, https://doi.org/10.1016/j.vacuum.2022.110972.

[56] S. Vernuccio, E.E. Bickel, R. Gounder, L.J. Broadbelt, Propene oligomerization on Beta zeolites: development of a microkinetic model and experimental validation, J. Catal. 395 (2021) 302–314, https://doi.org/10.1016/j.jcat.2021.01.018.

[57] J. Huang, L. Sementa, Z. Liu, G. Barcaro, M. Feng, E. Liu, L. Jiao, M. Xu, D. Leshchev, S.-J. Lee, M. Li, C. Wan, E. Zhu, Y. Liu, B. Peng, X. Duan, W. A. Goddard, Alessandro Fortunelli, Q. Jia, Y. Huang, Experimental Sabatier plot for predictive design of active and stable Pt-alloy oxygen reduction reaction catalysts, Nature Catalysis 5 (6) (2022) 513–523, https://doi.org/10.1038/s41929-022-00797-0.

[58] O. Mohan, Shambhawi Shambhawi, R. Xu, A.A. Lapkin, S.H. Mushrif, Investigating CO₂ Methanation on Ni and Ru: DFT assisted microkinetic analysis, ChemCatChem 13 (10) (2021) 2420–2433, https://doi.org/10.1002/cctc.202100073.

[59] B. Kreitz, G.D. Wehinger, C.F. Goldsmith, T. Turek, Microkinetic modeling of the transient CO₂ Methanation with DFT-based uncertainties in a Berty reactor, ChemCatChem 14 (18) (2022), https://doi.org/10.1002/cctc.202200570.

[60] K. Alexopoulos, M. John, K. Van der Borght, V. Galvita, M.-F. Reyniers, G. B. Marin, DFT-based microkinetic modeling of ethanol dehydration in H-ZSM-5, J. Catal. 339 (2016) 173–185, https://doi.org/10.1016/j.jcat.2016.04.020.

[61] E. Gutierrez-Acebo, J. Rey, Christophe Bouchy, Y. Schuurman, Céline Chizallet, Ethylcyclohexane Hydroconversion in EU-1 zeolite: DFT-based microkinetic modeling reveals the nature of the kinetically relevant intermediates, ChemCatChem 13 (15) (2021) 3434–3442, https://doi.org/10.1002/cctc.202100421.

[62] T. Choksi, J. Greeley, Partial oxidation of methanol on MoO_3 (010): A DFT and microkinetic study, ACS Catal. 6 (11) (2016) 7260–7277, https://doi.org/10.1021/acscatal.6b01633.

[63] E.F. Souza, Role of oxygen vacancies in CO2 Methanation over zirconia: A mechanistic DFT and microkinetic study, Surf. Sci. 746 (2024) 122500, https://doi.org/10.1016/j.susc.2024.122500.

[64] B.C. Dharmalingam, Ajay Koushik V, M. Mureddu, L. Atzori, S. Lai, A. Pettinau, N. S. Kaisare, Preeti Aghalayam, Jithin John Varghese, Unravelling the role of metal-metal oxide interfaces of Cu/ZnO/ZrO2/Al2O3 catalyst for methanol synthesis from CO2: insights from experiments and DFT-based microkinetic modeling, Appl. Catal. B Environ. Energy 332 (2023) 122743, https://doi.org/10.1016/j.apcatb.2023.122743.

[65] Žan Kovačič, Blaž Likozar, Matej Huš, Ab initio modelling of photocatalytic CO2 reduction reactions over cu/TiO2 semiconductors including the electronic excitation effects, Chem. Eng. J. 485 (2024) 149894, https://doi.org/10.1016/j.cej.2024.149894.

[66] A. Solé-Daura, Youven Benseghir, Minh-Huong Ha-Thi, M. Fontecave, P. Mialane, A. Dolbecq, C. Mellot-Draznieks, Origin of the boosting effect of polyoxometalates in photocatalysis: the case of CO_2 reduction by a Rh-containing metal–organic framework, ACS Catal. 12 (15) (2022) 9244–9255, https://doi.org/10.1021/acscatal.2c02088.

[67] C.N. Evrard, L.M. Thompson, Mechanistic origin of selective methane to methanol oxidation on vanadium-doped mesoporous amorphous silica Photocatalyst, J. Phys. Chem. C 127 (22) (2023) 10488–10498, https://doi.org/10.1021/acs.jpcc.3c00663.

[68] A.K. Sharma, Feliu Maseras, The subtle mechanism of nickel-Photocatalyzed C(sp^3)–H cross-coupling, Inorg. Chem. 63 (30) (2024) 13801–13806, https://doi.org/10.1021/acs.inorgchem.4c01763.

[69] X. Wu, X. Fan, S. Xie, I. Scodeller, X. Wen, D. Vangestel, J. Cheng, B. Sels, Zinc-indium-sulfide favors efficient C − H bond activation by concerted proton-coupled electron transfer, Nat. Commun. 15 (1) (2024), https://doi.org/10.1038/s41467-024-49265-2.

[70] G. Kresse, J. Furthmüller, Efficiency of ab-initio total energy calculations for metals and semiconductors using a plane-wave basis set, Comput. Mater. Sci. 6 (1) (1996) 15–50, https://doi.org/10.1016/0927-0256(96)00008-0.

[71] G. Kresse, J. Furthmüller, Efficient iterative schemes for ab initio total-energy calculations using a plane-wave basis set, Phys. Rev. B 54 (16) (1996) 11169–11186, https://doi.org/10.1103/physrevb.54.11169.

[72] J.P. Perdew, K. Burke, M. Ernzerhof, Generalized gradient approximation made simple, Phys. Rev. Lett. 77 (18) (1996) 3865–3868, https://doi.org/10.1103/physrevlett.77.3865.

[73] P.E. Blöchl, Projector augmented-wave method, Phys. Rev. B 50 (24) (1994) 17953–17979, https://doi.org/10.1103/physrevb.50.17953.

[74] G. Kresse, D. Joubert, From ultrasoft pseudopotentials to the projector augmented-wave method, Phys. Rev. B 59 (3) (1999) 1758–1775, https://doi.org/10.1103/physrevb.59.1758.

[75] S. Grimme, J. Antony, S. Ehrlich, H. Krieg, A consistent and accurate ab initio parametrization of density functional dispersion correction (DFT-D) for the 94 elements H-Pu, J. Chem. Phys. 132 (15) (2010) 154104, https://doi.org/10.1063/1.3382344.

[76] S. Grimme, S. Ehrlich, L. Goerigk, Effect of the damping function in dispersion corrected density functional theory, J. Comput. Chem. 32 (7) (2011) 1456–1465, https://doi.org/10.1002/jcc.21759.

[77] S.L. Dudarev, G.A. Botton, S.Y. Savrasov, C.J. Humphreys, A.P. Sutton, Electron-energy-loss spectra and the structural stability of nickel oxide: An LSDA+U study, Phys. Rev. B 57 (3) (1998) 1505–1509, https://doi.org/10.1103/physrevb.57.1505.

[78] G. Liu, Hua Gui Yang, J. Pan, Y. Yang, Gao Qing Lu, H.-M. Cheng, Titanium dioxide crystals with tailored facets, Chem. Rev. 114 (19) (2014) 9559–9612, https://doi.org/10.1021/cr400621z.

[79] J. He, Y. Du, Y. Bai, J. An, X. Cai, Y. Chen, P. Wang, X. Yang, Q. Feng, Facile formation of anatase/rutile TiO2 nanocomposites with enhanced photocatalytic activity, Molecules 24 (16) (2019) 2996, https://doi.org/10.3390/molecules24162996.

[80] S. Muniandy, S., Mohd Kaus, N.H., Jiang, Z.-T., Altarawneh, M. and Lee, H.L., Green synthesis of mesoporous anatase TiO2 nanoparticles and their photocatalytic activities, RSC Adv. 7 (76) (2017) 48083–48094, https://doi.org/10.1039/c7ra08187a.

[81] R. Martinez-Casado, G. Mallia, N.M. Harrison, Rubén Pérez, First-principles study of the water adsorption on Anatase(101) as a function of the coverage, J. Phys. Chem. C 122 (36) (2018) 20736–20744, https://doi.org/10.1021/acs.jpcc.8b05081.

[82] A. Vittadini, A. Selloni, F.P. Rotzinger, M. Grätzel, Formic acid adsorption on dry and hydrated TiO2 Anatase (101) surfaces by DFT calculations, J. Phys. Chem. B 104 (6) (2000) 1300–1306, https://doi.org/10.1021/jp993583b.

[83] A. Hemeryck, A. Motta, C. Lacaze-Dufaure, D. Costa, P. Marcus, DFT-D study of adsorption of diaminoethane and propylamine molecules on anatase (101) TiO2 surface, Appl. Surf. Sci. 426 (2017) 107–115, https://doi.org/10.1016/j.apsusc.2017.07.161.

[84] D.C. Sorescu, W.A. Al-Saidi, K.D. Jordan, CO2 adsorption on TiO2(101) anatase: a dispersion-corrected density functional theory study, J. Chem. Phys. 135 (12) (2011) 124701, https://doi.org/10.1063/1.3638181.

[85] F. Maldonado, D. Castillo, S. Aguilar, J. Carrión, Aramis Sánchez, Adsorption of CuSO4 on Anatase TiO2 (101) surface: a DFT study, Inorganics 13 (4) (2025) 114, https://doi.org/10.3390/inorganics13040114.

[86] A. Camilo, E. Flórez, F. Núñez-Zarur, Glycerol adsorption on TiO2 surfaces: a systematic periodic DFT study, ChemistryOpen (2025), https://doi.org/10.1002/open.202400153.

[87] G. Henkelman, H. Jónsson, Improved tangent estimate in the nudged elastic band method for finding minimum energy paths and saddle points, J. Chem. Phys. 113 (22) (2000) 9978–9985, https://doi.org/10.1063/1.1323224.

[88] D. Sheppard, R. Terrell, G. Henkelman, Optimization methods for finding minimum energy paths, J. Chem. Phys. 128 (13) (2008) 134106, https://doi.org/10.1063/1.2841941.

[89] V. Wang, N. Xu, J.-C. Liu, G. Tang, W.-T. Geng, VASPKIT: A user-friendly interface facilitating high-throughput computing and analysis using VASP code, Comput. Phys. Commun. 267 (2021) 108033, https://doi.org/10.1016/j.cpc.2021.108033.

[90] R. Islam, Foroogh Khezeli, S. Ringe, C. Plaisance, An implicit electrolyte model for plane wave density functional theory exhibiting nonlinear response and a nonlocal cavity definition, J. Chem. Phys. 159 (23) (2023), https://doi.org/10.1063/5.0176308.

[91] P. Pechukas, Transition state theory, Annu. Rev. Phys. Chem. 32 (1) (1981) 159–177, https://doi.org/10.1146/annurev.pc.32.100181.001111.

[92] C.T. Campbell, J.R.V. Sellers, Enthalpies and entropies of adsorption on well-defined oxide surfaces: experimental measurements, Chem. Rev. 113 (6) (2013) 4106–4135, https://doi.org/10.1021/cr300329s.

[93] A.H. Motagamwala, J.A. Dumesic, Microkinetic modeling: a tool for rational catalyst design, Chem. Rev. 121 (2) (2020) 1049–1076, https://doi.org/10.1021/acs.chemrev.0c00394.

[94] R. Ma, G. Williams, M. Muscetta, S. Vernuccio, Enhanced photocatalytic hydrogen evolution via ball-milled PtO2/TiO2 heterojunction photocatalyst: An alternative approach for efficient energy production, Chem. Eng. J. 507 (2025) 160228, https://doi.org/10.1016/j.cej.2025.160228.

[95] F. Lin, H. Wang, Y. Zhao, J. Fu, D. Mei, N.R. Jaegers, F. Gao, Y. Wang, Elucidation of active sites in aldol condensation of acetone over single-facet dominant Anatase TiO2 (101) and (001) catalysts, JACS Au 1 (1) (2020) 41–52, https://doi.org/10.1021/jacsau.0c00028.

[96] J. Xing, J.F. Chen, Y.H. Li, W.T. Yuan, Y. Zhou, L.R. Zheng, H.F. Wang, P. Hu, Y. Wang, H.J. Zhao, Y. Wang, H.G. Yang, Stable isolated metal atoms as active sites for photocatalytic hydrogen evolution, Chem. Eur. J. 20 (8) (2014) 2138–2144, https://doi.org/10.1002/chem.201303366.

[97] J. Xing, H.B. Jiang, J.F. Chen, Y.H. Li, L. Wu, S. Yang, L.R. Zheng, H.F. Wang, P. Hu, H.J. Zhao, H.G. Yang, Active sites on hydrogen evolution photocatalyst, J Mater Chem A 1 (48) (2013) 15258–15264, https://doi.org/10.1039/c3ta13167j.

[98] Y. Zhang, Y. Dai, H. Li, L. Yin, M.R. Hoffmann, Proton-assisted electron transfer and hydrogen-atom diffusion in a model system for photocatalytic hydrogen production, Communications Materials 1 (1) (2020), https://doi.org/10.1038/s43246-020-00068-0.

[99] Naresh Nalajala, K.N. Salgaonkar, I. Chauhan, Siva Prasad Mekala, C.S. Gopinath, Aqueous methanol to formaldehyde and hydrogen on Pd/TiO2 by Photocatalysis in direct sunlight: structure dependent activity of Nano-Pd and atomic Pt-coated counterparts, ACS Appl Energy Mater 4 (11) (2021) 13347–13360, https://doi.org/10.1021/acsaem.1c03080.

[100] K.R. Phillips, S.C. Jensen, M. Baron, S.-C. Li, C.M. Friend, Sequential photo-oxidation of methanol to methyl formate on TiO2(110), J. Am. Chem. Soc. 135 (2) (2012) 574–577, https://doi.org/10.1021/ja3106797.

[101] X. Lang, B. Wen, C. Zhou, Z. Ren, L.-M. Liu, First-principles study of methanol oxidation into methyl Formate on rutile TiO2(110), J. Phys. Chem. C 118 (34) (2014) 19859–19868, https://doi.org/10.1021/jp505674g.

[102] J. Wang, B. Zhang, W. Guo, L. Wang, J. Chen, H. Pan, W. Sun, Toward Electrocatalytic methanol oxidation reaction: longstanding debates and emerging catalysts, Adv. Mater. 35 (26) (2023), https://doi.org/10.1002/adma.202211099.

[103] J. Zhang, C. Peng, H. Wang, P. Hu, Identifying the role of Photogenerated holes in photocatalytic methanol dissociation on rutile TiO2(110), ACS Catal. 7 (4) (2017) 2374–2380, https://doi.org/10.1021/acscatal.6b03348.

[104] X.-P. Tao, X.-Q. Gong, D. Wang, Photocatalytic cleavage of C–H bonds: a case study of formaldehyde photodegradation from density functional theory, J. Phys. Chem. C 127 (42) (2023) 20652–20661, https://doi.org/10.1021/acs.jpcc.3c04538.

[105] W.-N. Zhao, Z.-P. Liu, Mechanism and active site of photocatalytic water splitting on titania in aqueous surroundings, Chem. Sci. 5 (6) (2014) 2256–2264, https://doi.org/10.1039/c3sc53385a.

[106] D. Zhang, Visible light-induced photocatalysis through surface plasmon excitation of platinum-metallized titania for photocatalytic bleaching of rhodamine B, Monatshefte für Chemie - Chemical Monthly 143 (5) (2011) 729–738, https://doi.org/10.1007/s00706-011-0631-2.

[107] D. Zhang, S.-W. Lee, Photocatalytic activity of ag, au-deposited TiO2 nanoparticles prepared by sonochemical reduction method, Surf. Rev. Lett. 17 (01) (2010) 21–26, https://doi.org/10.1142/s0218625x10013588.

[108] J. Kaur, R. Singh, B. Pal, Influence of coinage and platinum group metal co-catalysis for the photocatalytic reduction of m-dinitrobenzene by P25 and rutile

TiO2, J. Mol. Catal. A Chem. 397 (2015) 99–105, https://doi.org/10.1016/j.molcata.2014.11.007.

[109] D. Wang, T. Sheng, J. Chen, H.-F. Wang, P. Hu, Identifying the key obstacle in photocatalytic oxygen evolution on rutile TiO2, Nat. Catal. 1 (4) (2018) 291–299, https://doi.org/10.1038/s41929-018-0055-z.

[110] T.L. Thompson, J.T. Yates, Monitoring hole trapping in Photoexcited TiO2(110) using a surface photoreaction, J. Phys. Chem. B 109 (39) (2005) 18230–18236, https://doi.org/10.1021/jp0530451.

[111] V. Meinhardová, L. Dubnová, H. Drobná, L. Matějová, K. Kočí, L. Čapek, Role of lamp type in conventional batch and micro-photoreactor for photocatalytic hydrogen production, Front. Chem. 11 (2023), https://doi.org/10.3389/fchem.2023.1271410.

[112] G. Pirgholi-Givi, S. Farjami-Shayesteh, Y. Azizian-Kalandaragh, The influence of irradiation intensity and stirring rate on the photocatalytic activity of titanium dioxide nanostructures prepared by the microwave-assisted method for photodegradation of MB from water, Phys. B Condens. Matter 578 (2020) 411886, https://doi.org/10.1016/j.physb.2019.411886.

[113] T.D. Svejstrup, A. Chatterjee, D. Schekin, T. Wagner, J. Zach, M.J. Johansson, G. Bergonzini, B. König, Effects of light intensity and reaction temperature on photoreactions in commercial Photoreactors, ChemPhotoChem 5 (9) (2021) 808–814, https://doi.org/10.1002/cptc.202100059.

[114] L. Clarizia, I.D. Somma, L. Onotri, R. Andreozzi, R. Marotta, Kinetic modeling of hydrogen generation over nano-cu (s) /TiO 2 catalyst through photoreforming of alcohols, Catal. Today 281 (2017) 117–123, https://doi.org/10.1016/j.cattod.2016.05.053.

[115] M. Muscetta, L. Clarizia, C. Garlisi, G. Palmisano, R. Marotta, R. Andreozzi, I. Di Somma, Hydrogen production upon UV-light irradiation of cu/TiO2 photocatalyst in the presence of alkanol-amines, Int. J. Hydrog. Energy 45 (51) (2020) 26701–26715, https://doi.org/10.1016/j.ijhydene.2020.07.002.

[116] Y. Wang, B. Wen, Arjun Dahal, G.A. Kimmel, R. Rousseau, Annabella Selloni, N.G. Petrik, Zdenek Dohnálek, Binding of formic acid on Anatase TiO2(101), J. Phys. Chem. C 124 (37) (2020) 20228–20239, https://doi.org/10.1021/acs.jpcc.0c06031.

[117] K.J.A. Raj, A.V. Ramaswamy, B. Viswanathan, Surface area, pore size, and particle size engineering of Titania with seeding technique and phosphate modification, J. Phys. Chem. C 113 (31) (2009) 13750–13757, https://doi.org/10.1021/jp902468v.

[118] M. Bursch, J. Mewes, A. Hansen, S. Grimme, Best-practice DFT protocols for basic molecular computational chemistry, Angew. Chem. Int. Ed. 61 (42) (2022), https://doi.org/10.1002/anie.202205735.

[119] L. Liu, X. Chen, Titanium dioxide nanomaterials: self-structural modifications, Chem. Rev. 114 (19) (2014) 9890–9918, https://doi.org/10.1021/cr400624r.

[120] W.E. Stewart, M. Caracotsios, J.P. Sorensen, *Double Precision Differential-Algebraic Sensitive Analysis Code,* Version 1997 vol. 3, Wisconsin University, Madison, WI, 1997.

[121] W.E. Stewart, M. Caracotsios, J.P. Sorensen, *Generalized Regression Software (GREG),* Version 1997 vol. 3, Wisconsin University, Madison, WI, 1997.